

Chapter 4

Multi-scale modelling of dry granular flows

4.1 Introduction

In nature, instabilities of slopes or cliffs are dramatic events involving sudden release of a large mass of soil. However, the prediction of catastrophic events still represents challenge, one difficulty being our incomplete understanding of the dynamics of granular flows (Rondon et al., 2011). Understanding the mechanics is of particular importance for risks assessment. Small scale laboratory experiments are usually unable to properly capture the dynamics of geophysical events. However, they can be useful to precisely study physical mechanisms, which may play a role in real flows (Iverson, 1997).

Conventionally, granular materials such as soils are modelled as a continuum. On a macroscopic scale, granular materials exhibit many collective phenomena and the use of continuum mechanics to describe the macroscopic behaviour can be justified. However, on a grain scale, the granular materials exhibit complex solid-like and/or fluid-like behaviour depending on how the grains interact with each other. Numerical studies at grain scale allows a precise understanding of the internal flow structure. Recent works on granular materials suggest that a continuum law may be incapable of revealing in-homogeneities at the grain-scale level, such as orientation of force chains, which are purely due to micro-structural effects Rycroft et al. (2009). Discrete Element approaches are capable of simulating the granular material as a discontinuous system allowing one to probe into local variables such as position, velocities, contact forces, etc. The fundamental question is how to model granular materials which exhibit complex phenomenon. It is important to understand the mechanics of granular flows and the ability and limitations of continuum methods in capturing the flow dynamics.

¹ 4.2 Granular column collapse

² The collapse of a granular column, which mimics the collapse of a cliff, has been extensively
³ studied in the case of dry granular material (Hogg, 2007; Kerswell, 2005; Lajeunesse et al.,
⁴ 2004; Lo et al., 2009; Lube et al., 2005; Staron and Hinch, 2007; Zenit, 2005). The granular
⁵ column collapse experiment involves filling a rectangular channel of height H_0 and width L_0
⁶ with a granular material of mass ‘m’ (see figure 4.1). The granular column is then released
⁷ *en masse* by quickly removing the gate, thus allowing the granular material to collapse onto
⁸ the horizontal surface, forming a deposit having a final height H_f and length L_f . Despite the
⁹ complexity of the intermediate flow dynamics, experimental investigations have shown that the
¹⁰ flow evolution, the spreading velocity, the final extent of the deposit, and the energy dissipation
¹¹ can be scaled in a quantitative way independent of the substrate properties, grain size, density,
¹² and shape of the granular material and released mass (Lajeunesse et al., 2005; Lube et al., 2005;
¹³ Staron and Hinch, 2007). The granular collapse has also been studied using discrete element
¹⁴ method, which allows precise measurement of the internal flow structure (Lo et al., 2009;
¹⁵ Staron and Hinch, 2006, 2007; Utili et al., 2014). Power laws relating the final run-out and
¹⁶ height to the initial aspect ratio of the column were observed. These findings immediately pose
¹⁷ the question: are these simple scaling fortuitous, an oversimplification, or in fact indicative of a
¹⁸ simple dynamical balance?

¹⁹ Granular flows are conventionally modelled as a frictional dissipation process in continuum
²⁰ mechanics but the lack of influence of inter-particle friction on the energy dissipation and
²¹ spreading dynamics (Lube et al., 2005) is surprising. However, Kerswell (2005) showed the run-
²² out behaviour has a clear material dependence, which corroborates the conclusion of Lajeunesse
²³ et al. (2004) and softens that of Lube et al. (2005). The collapse of a granular column on a
²⁴ horizontal surface is a simple case of granular flow, however a proper model that describes
²⁵ the flow dynamics is still lacking. Simple mathematical models based on conservation of
²⁶ horizontal momentum capture the scaling laws of the final deposit, but fail to describe the initial
²⁷ transition regime. From a theoretical point of view, the spreading has been described using
²⁸ depth averaged equations (Kerswell, 2005; Larrieu et al., 2006). The depth-averaged and Saint-
²⁹ Venant equations struggle to recover the precise dynamic behaviour of the system (Warnett
³⁰ et al., 2013) and only succeeds in predicting the scaling observed for aspect ratio less than one.
³¹ However, describing larger aspect ratio and capturing the initial stage of the collapse, when
³² the grains experience a rapid change of direction from vertical to horizontal, remain an open
³³ challenge,

³⁴ In the present study, multi-scale numerical modelling, i.e. grain-scale modelling and
³⁵ continuum analyses, of the quasi-two dimensional collapse of granular columns are performed
³⁶ using Discrete Element (DEM) approach and Generalised Interpolation Material Point Method

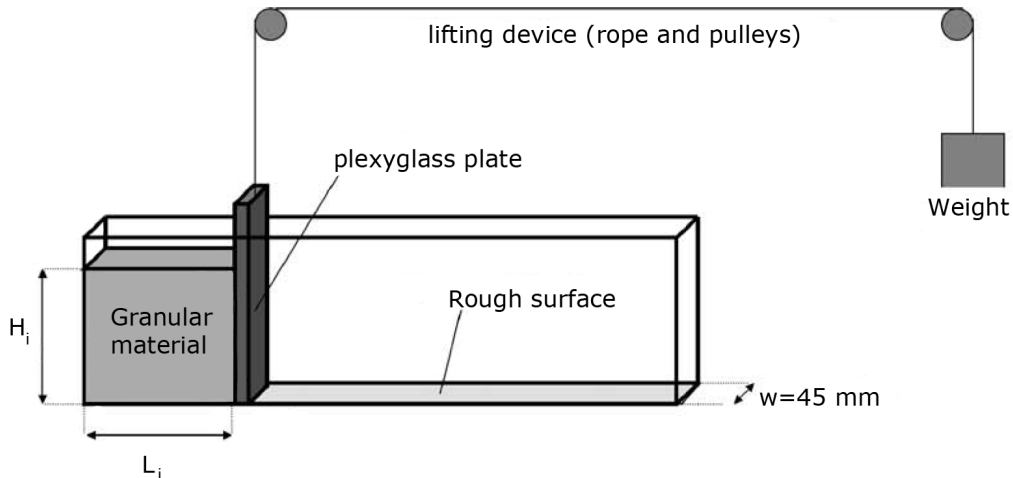


Figure 4.1 Schematic of experimental configuration for 2-D collapse in a rectangular channel, ([Lajeunesse et al., 2004](#))

(GIMPM). GIMPM, a hybrid Eulerian – Lagrangian approach, with Mohr-Coloumb failure criterion is used to describe the continuum behaviour of granular column collapse. While the micro-mechanics of the flow is captured using DEM simulations. Comparing the grain scale behaviour with the continuum simulations highlights the limitations of continuum approaches in modelling the dense granular flows and their ability (or lack thereof) in capturing the complex micro-scale rheology.

4.2.1 Numerical set-up

In this study, numerical simulations of granular columns are analogous to the experimental investigation of column collapse performed by [Lajeunesse et al. \(2004\)](#). The experimental configuration of [Lajeunesse et al. \(2004\)](#) is shown in figure 4.1. Granular material of mass ' M ' was poured into a container to form a rectangular heap of length ' L_0 ', height ' H_0 ' and thickness ' W '. The internal friction angle and the wall friction between the wall and the glass beads measured by [Lajeunesse et al. \(2004\)](#) are listed in table 4.1. The gate was then quickly removed to release the granular mass that spreads in the horizontal channel until it comes to rest. The final run-out distance ' L_f ' and the collapsed height ' H_f ' were measured. The run-out distance and collapse height exhibit a power law relation with the initial aspect ratio ' a ' ($= H_0/L_0$) of the column.

Granular materials when released suddenly on a horizontal surface exhibit transient flow. In this study, the mechanism of flow initiation, spreading dynamics and energy dissipation are studied for varying initial aspect ratios of the granular column. DEM soil grain characteristics match that of the experiment. The particle size distribution (PSD) is one of the most impor-

Table 4.1 Material properties of glass ballotini ([Lajeunesse et al., 2004](#))

Parameter	Value
Mean diameter	1.15 mm
Repose angle	$22 \pm 0.5^\circ$
Avalanche angle	$27.4 \pm 0.5^\circ$
Wall friction angle	$24.8 \pm 0.2^\circ$

tant factors controlling landslide initiation and soil permeability. Cumulative β distribution (described in ??) is used to generate a graded sample with a mean grain diameter of 1.15mm (see figure 4.2b). The DEM sample is composed of ~ 3000 disks with a uniform distribution of diameters by volume fractions in the range $[d_{min}, d_{max}] = 0.92 - 1.38$ mm with polydispersity $r = \frac{d_{max}}{d_{min}} = 1.5$. The granular column is prepared by allowing the randomly placed grains to undergo ballistic deposition with a constant potential head between layers of soil grains. A snapshot of the sample generated is shown in figure 4.2a. A DEM sample with soil grains arranged in a regular hexagonal lattice is also used to study the influence of crystallisation and jamming on the run-out behaviour.

The overlap between grains are determined by the stiffness k_n of the spring in the normal direction. Typically, an average overlap in the range 0.1 to 1.0% is desirable [Zenit \(2005\)](#) and the spring constant is chosen to produce grain overlaps in this range. The stiffness is determined as

$$k_n = \frac{2\pi G}{(1-\nu)[2\ln(\frac{2r}{A}) - 1]} \quad (4.1)$$

$$A = \left[\frac{2r(1-\nu)f_n}{\pi G} \right]^{\frac{1}{2}}, \quad (4.2)$$

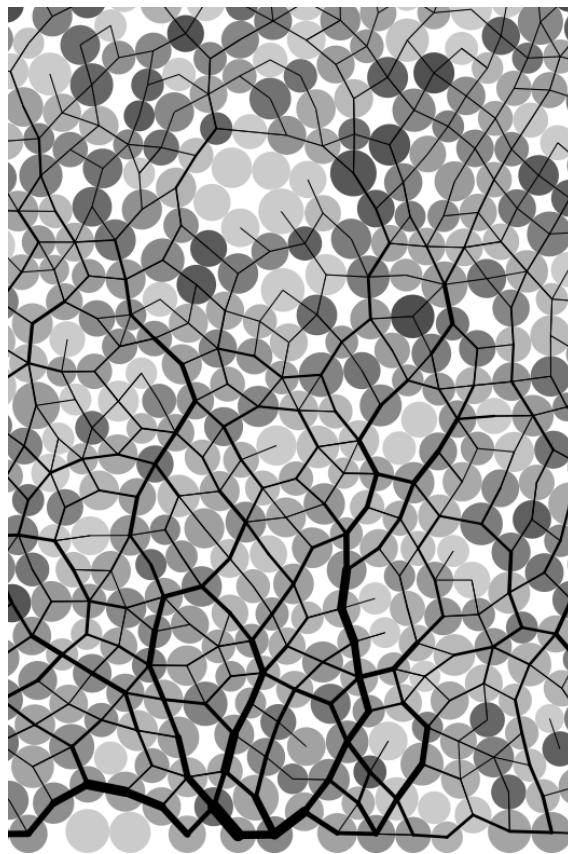
where f_n is the normal contact force; G is the shear modulus; ν is the Poisson's ratio and r is the radius of the grain. A simpler form of stiffness for a spherical grain is defined as

$$k_n = 4ER, \quad (4.3)$$

where E is the Young's modulus of the material and R is the radius of the grain. [Cambou et al. \(2009\)](#) observed that the contact model has negligible influence on the run-out behaviour of rapid granular flows. The granular collapse simulations performed using non-linear Hertz-Mindlin contact model and the linear-elastic contact model showed no significant difference on the granular flow behaviour [Utili et al. \(2014\)](#). Linear-elastic contact model is used in the

4.2 Granular column collapse

5



(a) DEM sample prepared using ballistic deposition

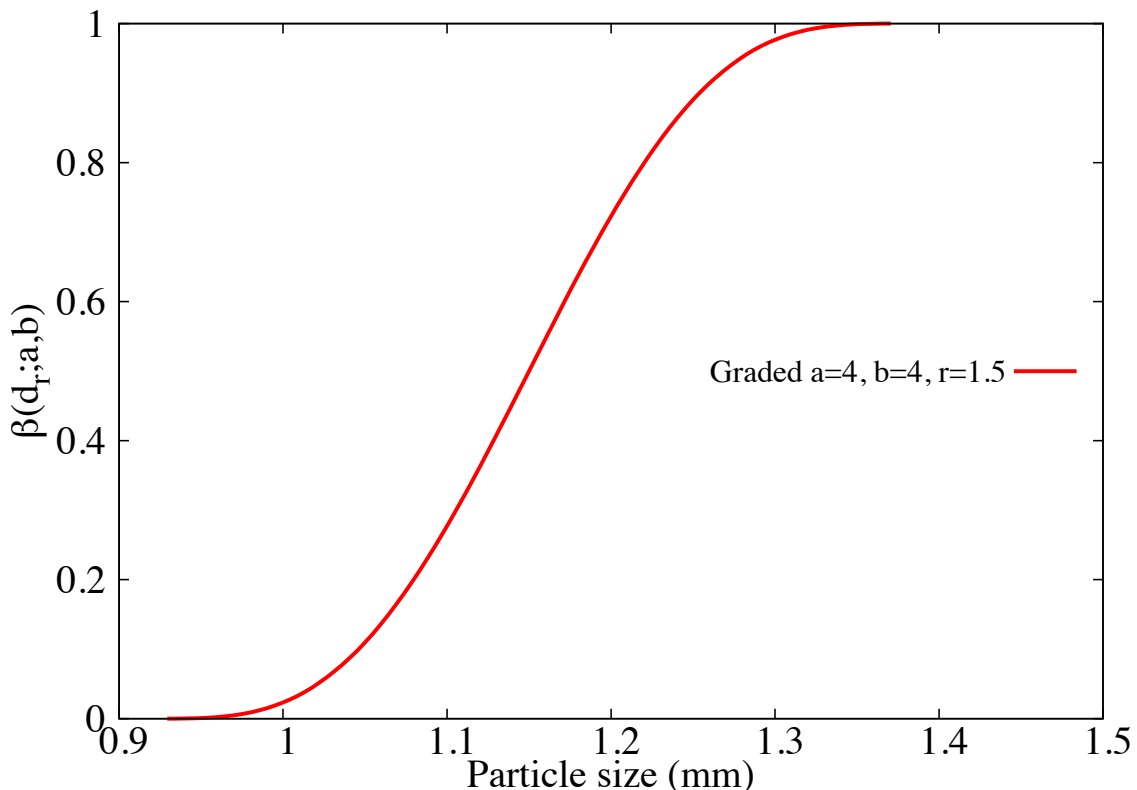
(b) DEM grains generated using the cumulative β distribution

Figure 4.2 DEM sample characteristics

Table 4.2 Micro-mechanical parameters used in DEM simulations

Parameter	Value
Young's modulus of glass bead	$70 \times 10^9 \text{ N m}^{-2}$
Poisson's ratio	0.22 - 0.24
Diameter of glass beads	0.92 to 1.38 mm
Normal and shear stiffness of grains	$1.6 \times 10^8 \text{ N m}^{-1}$
Normal and shear stiffness of wall	$4 \times 10^8 \text{ N m}^{-1}$
Inter-particle friction coefficient, μ	0.53
Wall friction coefficient	0.466
Coefficient of restitution, ϵ	0.755

¹ present study due to its simplicity and lower computation time requirement. The maximum
² tangential force is limited by the Mohr-Coloumb criterion.

³ [Staron and Hinch \(2006\)](#) observed that the coefficient of restitution ϵ was dramatically
⁴ changing the behaviour of the systems for $\epsilon \rightarrow 1$; in particular, this dramatic change is
⁵ expected to become more important for increasing values of a . On the contrary, for $\epsilon \leq 0.8$,
⁶ the influence of the coefficient of restitution becomes negligible. In the present study, a value
⁷ of 0.75 is adopted as the coefficient of restitution, similar values of restitution coefficient
⁸ was adopted by [Girolami et al. \(2012\)](#); [Zenit \(2005\)](#). The normal damping coefficient C_n is
⁹ appropriately chosen to achieve the required coefficient of restitution ϵ :

$$\text{10} \quad C_n = 2\gamma\sqrt{m_{ij}k_n} \quad (4.4)$$

$$\text{11} \quad \text{where } \gamma = -\frac{\ln(\epsilon)}{\sqrt{\pi^2 + \ln^2(\epsilon)}}, \quad \text{and} \quad m_{ij} = \frac{m_i m_j}{m_i + m_j}. \quad (4.5)$$

¹³ The micro-mechanical parameters used in this study are presented in table 4.2. Due to the
¹⁴ unsteady nature of the flow, the grains get dispersed on the horizontal plane as discrete bodies
¹⁵ start to separate from the main mass, hence the run-out distance is calculated as the position of
¹⁶ the farthest grain which has at least one contact with the main mass.

¹⁷ GIMPM with Mohr-Coloumb constitutive model is used to simulate plane strain collapse
¹⁸ of granular columns. [Crosta et al. \(2009\)](#) observed that the Mohr-Coloumb with non-associate
¹⁹ flow rule is able to capture granular collapse dynamics and models the strong vertical motion
²⁰ components, but it does not suffer the limitations of typical shallow water equation methods.
²¹ In order to understand the ability and limitations of continuum approaches in capturing the
²² local rheology, it is important to scale the grain scale properties, such as inter-particle friction
²³ and stiffness, to the continuum scale (macroscopic friction and Young's modulus). [Crosta et al.](#)
²⁴ ([2009](#)) observed that the friction angle plays a significant role on the run-out behaviour. In

4.2 Granular column collapse

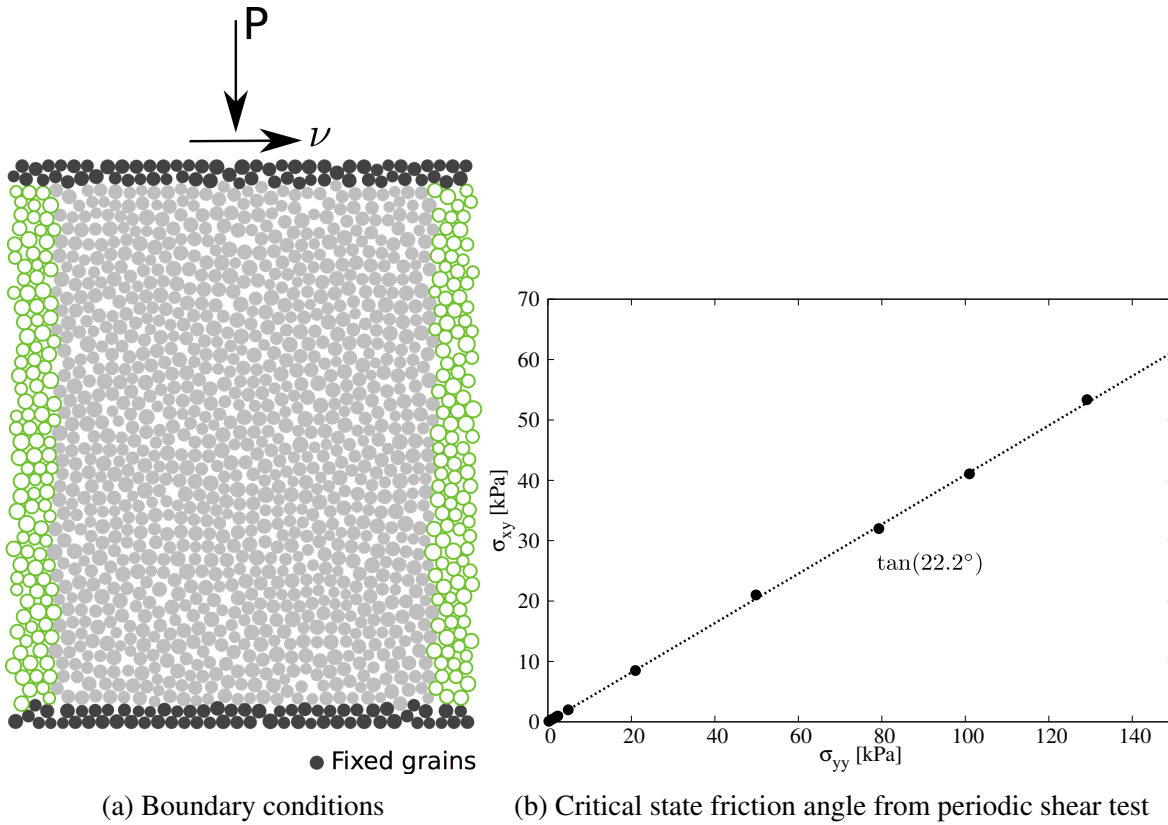


Figure 4.3 Periodic shear test

MPM simulations, the granular flow is assumed to be in critical state and the critical state friction angle is used in the Mohr-Coloumb model. In order to obtain the critical state friction angle of the granular sample, a shear test is performed using 1078 DEM grains. A bi-periodic boundary condition is adopted on the sides of the sample (see figure 4.3a). Two layers of fixed grains (shown in black) is placed at the top and the bottom of the shear sample. A normal pressure ‘P’ and a horizontal velocity v is applied to the fixed grains at the top of the shear sample. The normal effective stress is varied in the sample and the average shear stress of the sample is measured. The sample was sheared until critical state was reached. The slope of shear stress versus normal effective stress gives the critical state friction angle. A critical state friction angle of 22.2° is obtained. The macroscopic friction angle is in the range observed by Estrada et al. (2008); Mitchell and Soga (2005). The Young’s modulus of the granular assembly is obtained as the initial slope of the stress-strain plot of a uni-axial compression of a granular column using DEM.

Guilkey et al. (2003) suggests using at least four material points per cell for large deformation problems. In the present study, 16 material points per cell is adopted. If the mesh is too fine and the number of particles is too large, the particle size $2l/p$ decreases, and the GIMPM

Table 4.3 Parameters used in continuum simulations

Parameter	Value
Material point spacing	0.575 mm
Number of material points per cell	16
Young's Modulus, E	1.98×10^6 Pa
Poisson's ratio, ν	0.22 to 0.24
Friction angle, ϕ	$23.2 \pm 0.2^\circ$
Dilatancy angle, Φ	0°
Density, ρ	1800 kg m^{-3}
Wall friction	0.466
Time step increment	1.0×10^{-6} s

¹ interpolation function tends to approach the original MPM function, as shown by [Bardenhagen and Kober \(2004\)](#). Hence GIMPM loses the merit that it reduces the numerical noise due to material points crossing the background mesh. In addition, the probability of particles crossing the background mesh increases with decrease in mesh size, hence, more noise can be produced [Abe et al. \(2013\)](#). The effect of number of material points per cell on the run-out behaviour is discussed in section 4.3.5. Each material point represents one-fourth of a DEM soil grain. The parameters used for the continuum analyses are presented in table 4.3.

4.2.2 Deposit morphology

MPM and DEM simulations of granular column collapse are performed by varying the initial aspect ratio of the column. The evolution of the normalized final run-out distance, $\Delta L = (L_f - L_0)/L_0$, with the initial aspect ratio 'a' of the column is presented in figure 4.4. Similar to the experimental results, a power law relationship is observed between the normalized run-out distance and the initial aspect ratio of the column. In the present study, the following scaling law for the run-out is observed.

$$\frac{L_f - L_0}{L_0} \approx \begin{cases} 1.67a, & a \lesssim 2.3 \\ 2.5a^{2/3}, & a \gtrsim 2.3 \end{cases} \quad (4.6)$$

The normalised run-out distance predicted using DEM simulations are very close to the run-out observed in the experiments. DEM simulations with hexagonal packing estimates lower run-out distances in comparison with randomly packed sample. This can be attributed to the crystallisation and jamming effects in hexagonal packing. The small difference in the final run-out between DEM and experimental results can be attributed to the variation in the packing

4.2 Granular column collapse

9

of grains in the granular column. Also, the experimental data corresponds to granular column collapse in a rectangular channel, the collapse is not a pure two-dimensional collapse as in the case of numerical simulations. This can cause some variation in the run-out distance.

[Balmforth and Kerswell \(2005\)](#) observed that the material property affects the final run-out distance and included a pre-factor ‘ λ ’ in the scaling law, which is in contrast to the observation made by [Lube et al. \(2005\)](#). The scaling law observed in the present study for the random packing is identical to the scaling law observed by [Lajeunesse et al. \(2004\)](#), except for the pre-factor in the scaling law, indicating a strong correlation between the run-out distance and the material property. [Daerr and Douady \(1999\)](#) also observed the effect of initial packing density and the internal structure on the behaviour of granular flows. The continuum description of the granular column collapse using Material Point Method shows good agreement with the experimental results for columns with lower aspect ratio (‘ a ’ $\lesssim 2.3$), however it exhibits a significant increase in the run-out distance beyond the aspect ratio of 2.3. [Bandara \(2013\)](#) also observed a jump in the run-out distance at the initial aspect ratio of 2.

[Daerr and Douady \(1999\)](#) also proposed an interpretation in terms of active Coulomb yielding to account for their experimental observation of the transient granular surface flow occurring when a highly compacted cylindrical pile of granular media supported by a disc is suddenly released and crumbles to form a cone.

[Staron and Hinch \(2006\)](#) observed influence of role of friction. We first observed that the coefficient of restitution e was dramatically changing the behaviour of the systems for $e \rightarrow 1$; in particular, this dramatic change is expected to become more important for increasing values of a . On the contrary, for $e \leq 0.8$, the influence of the coefficient of restitution becomes negligible.

For small aspect ratio, the spreading results from a Coulomb-like failure of the edges and imply no free fall of the column. In this case, the effective friction properties of the flow can be simply predicted from the shape of the final deposit

In order to understand the mechanism of the run-out in a granular column collapse, it is essential to study the relation between the final collapsed height of the granular column and its initial aspect ratio. figure 4.5 shows the variation of the normalized final height with the initial aspect ratio of the column. The final height predicted by the DEM and the MPM simulations matches the experimental data for granular columns with aspect ratio below 0.7, which indicates that the initial density of the column has negligible effect on the final collapse height. The scaling of final height of the column with the initial aspect ratio of the column can

¹ be written as:

$$\frac{H_f}{L_i} \propto \begin{cases} a, & a \lesssim 0.7 \\ a^{2/3}, & a \gtrsim 0.7 \end{cases} \quad (4.7)$$

⁴ The Material Point Method predicts a higher final height of the column in comparison with
⁵ the particular simulations that should result in shorter run-outs, however it is inconsistent with
⁶ the observations. In case of granular columns with smaller aspect ratios, only a tiny portion of
⁷ the total mass is mobilized and the rest remains static, thus predicting the final collapse height
⁸ accurately. The final height of a column is controlled by the amount of static region in the
⁹ granular column collapse, while the run-out distance is essentially a function of the flowing
¹⁰ mass. Hence, it is essential to compare the evolution of flow and the internal flow structure
¹¹ in the Discrete Element Method and Material Point Method simulations to understand the
¹² limitations of both the continuum and discrete element approaches.

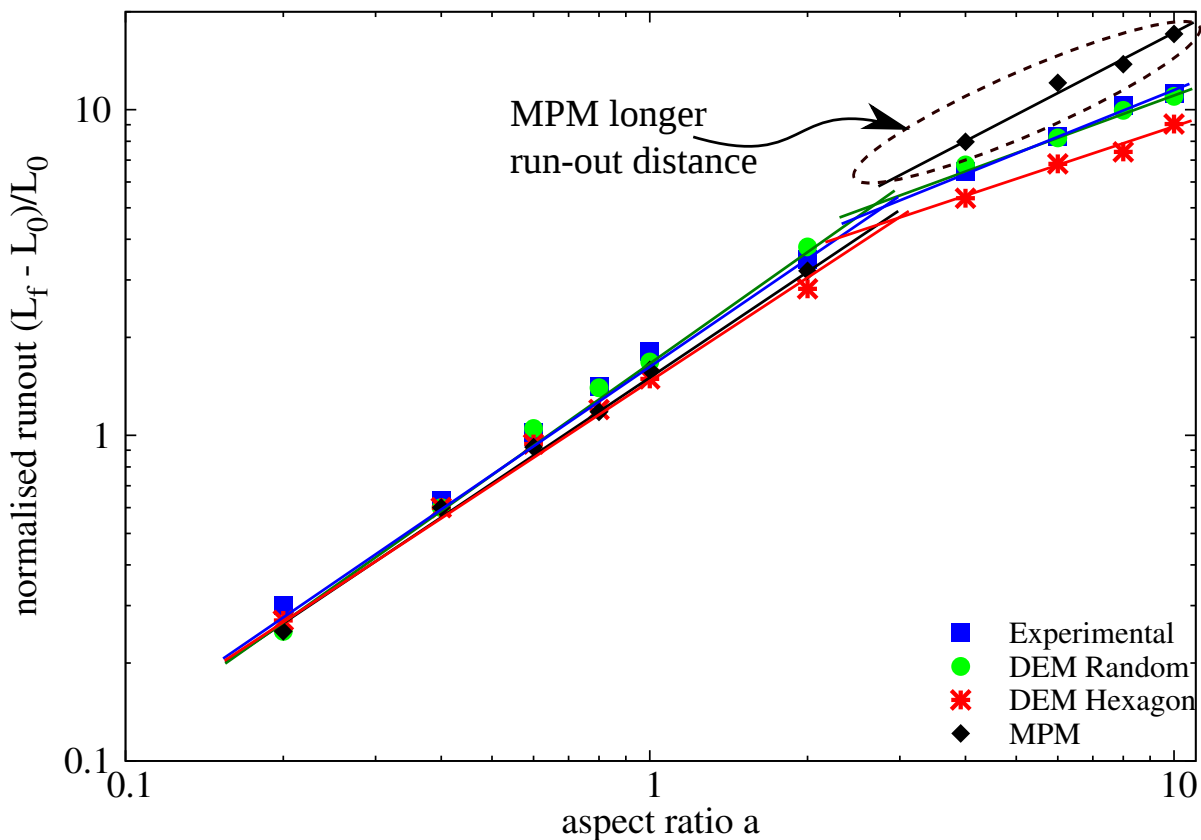


Figure 4.4 Normalised final run-out distance for columns with different initial aspect ratio

¹³ For large aspect ratios, in which we were mainly interested, the dissipation process is more
¹⁴ complex due to the free-fall dynamics. Indeed the vertical acceleration of the grains induces

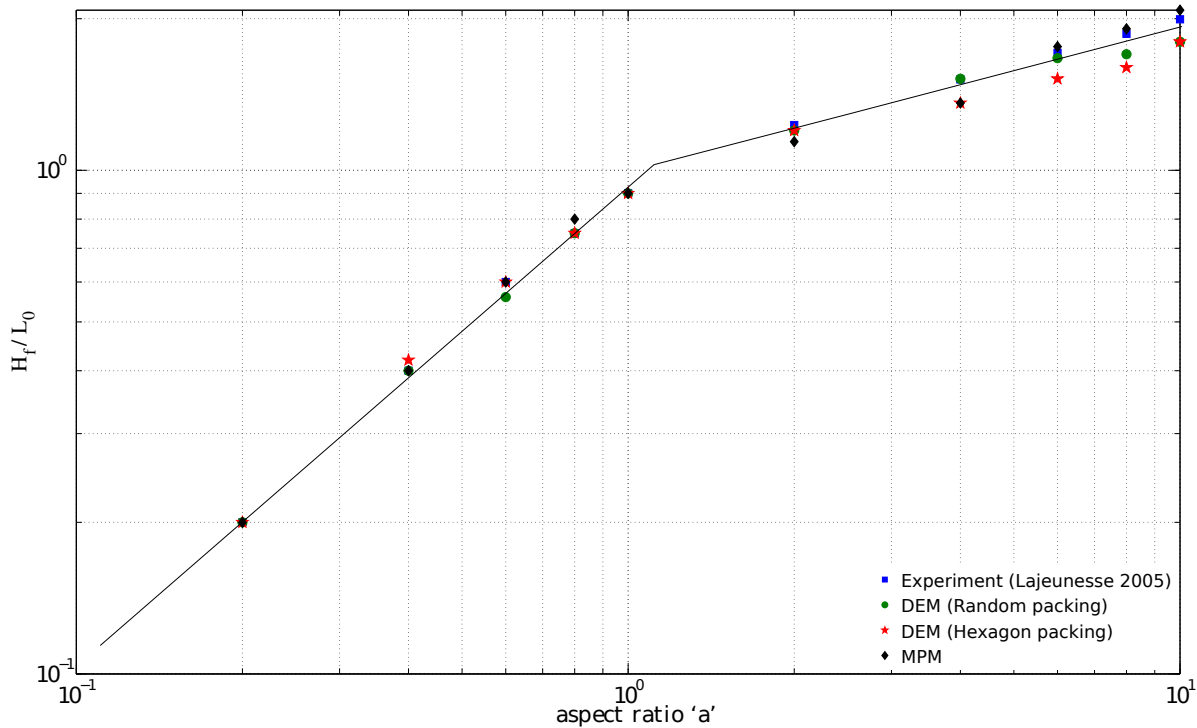


Figure 4.5 Normalised final collapse height for columns with different initial aspect ratio

a non-trivial mass distribution in the flow while propagating. This mass distribution plays a dominant role in the power-law scaling law obeyed by the run-out.

4.2.3 Flow evolution and internal flow structure

For a fixed granular material and substrate properties, the flow dynamics and the final deposit morphology do not depend on the volume of granular material released, but depend only on the aspect ratio ‘ a ’ of the column. A power law relationship is observed between the run-out distance and the initial aspect ratio of the column. A transition in the run-out behaviour at an aspect ratio of 2.3 indicates a change in the flow dynamics. For smaller aspect ratios, the granular mass fails through avalanching of flanks producing a truncated cone-like deposit ($‘a’ < 0.7$) or conical deposit ($‘a’ > 0.7$). At smaller values of aspect ratios, the flow is initiated by failure at the edge of the pile along a well-defined fracture surface. The grains located above the failure surface move “*en masse*” leaving a static region underneath the failure surface. After a transient time of order τ_c , defined as $\sqrt{H_i/g}$, the flow is fully developed. The velocity profile along the granular column at critical time τ_c is presented in figure 4.6. At critical time, the velocity field depends only on the position of the grain along the sliding mass. The maximum velocity is observed at the front of the flowing mass corresponding to that of a plug flow in

1 horizontal direction. Particulate and continuum simulations yield similar run-out distance
2 at critical time. Unlike particulate simulations, the Material point method predicts that the
3 maximum horizontal velocity occurs at the top of the sliding mass. Behind the fast flowing
4 front, the flow is localized in the mass above the failure surface and the velocity profiles are
5 locally parallel to the failure plane. The flow is composed of upper linear part and a lower
6 exponential tail in the static granular bed. The velocity profile is similar to steady granular
7 surface flow as observed by [Lajeunesse et al. \(2004\)](#).

8 For columns with lower initial aspect ratios, the run-out distance is proportional to the
9 mass flowing above the failure surface. To understand the amount of mass mobilized during a
10 collapse, the angle of the failure surface has to be studied. figure 4.6 shows a distinct failure
11 surface when the flow is fully developed at critical time τ_c . The angle of the failure surface is
12 found to be about 55° . The failure surface begins from the toe of the column and protrudes
13 inwards at an angle of 50 to 55° . For columns with lower aspect ratios, the formation of
14 the “truncated conical deposit” or “conical deposit” depends only on the initial length of the
15 column, as the angle of the failure surface is found to be independent of the aspect ratio. The
16 failure angle is consistent with the interpretation in terms of *active Coulomb failure* ([Lajeunesse et al., 2004](#)), which leads to a predicted failure angle $\theta_y = 45^\circ + \delta/2$, where δ is the internal
17 friction angle of the granular material. In the present study, the friction angle of the glass
18 beads is 22° , which leads to $\theta_y = 45^\circ + 22^\circ/2 = 56^\circ$, which is in good agreement with the
19 numerical simulations and experimental observations by [Lajeunesse et al. \(2004\)](#). Contrary to
20 the suggestion of [Lajeunesse et al. \(2004\)](#), the fracture angle is found to have no direct effect
21 on the transition between the truncated cone and the conical deposit occurring at an aspect ratio
22 of 0.7. [Schaefer \(1990\)](#) observed the onset of instabilities in a narrow wedges of 56 to 65° for
23 Cambridge type constitutive models that describes granular flows. This observation matches
24 well with the failure angle observed in the present study. The final profile of the collapsed
25 granular column with an initial aspect ratio of 0.4 is shown in figure 4.7. The failure surface is
26 distinct and the hexagonal dense packing of grains has a steeper failure surface in comparison
27 with the random packing. The variation observed in the angle of the failure surface causes a
28 difference in the amount of mobilized mass above the failure surface, and in turn in the run-out
29 distance. The lower value of run-out distance observed in the case of hexagonal packing of
30 grains can be attributed to the crystallisation effects. crystallisation is the formation of large-
31 scale lattice structures during the flow, resulting in non-generic flow patterns. crystallisation is
32 found to have a significant effect on the final state of the granular column. [Lacaze and Kerswell \(2009\)](#)
33 observed that poly-disperse grains have lesser tendency to crystallize especially in the
34 case of columns with larger aspect ratio.

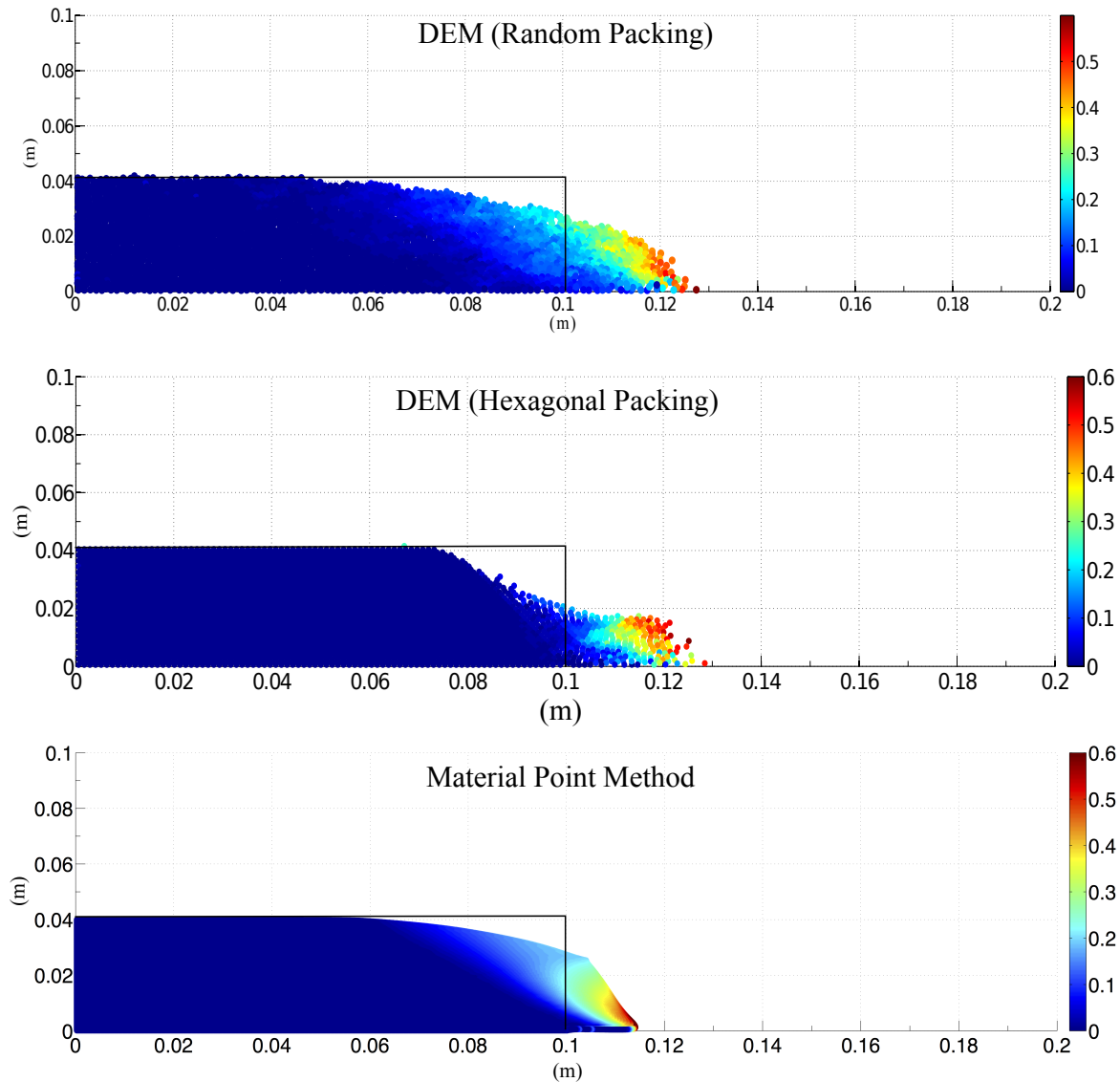


Figure 4.6 Velocity profile of a granular column collapse ($a' = 0.4$ & $t = \tau_c$)

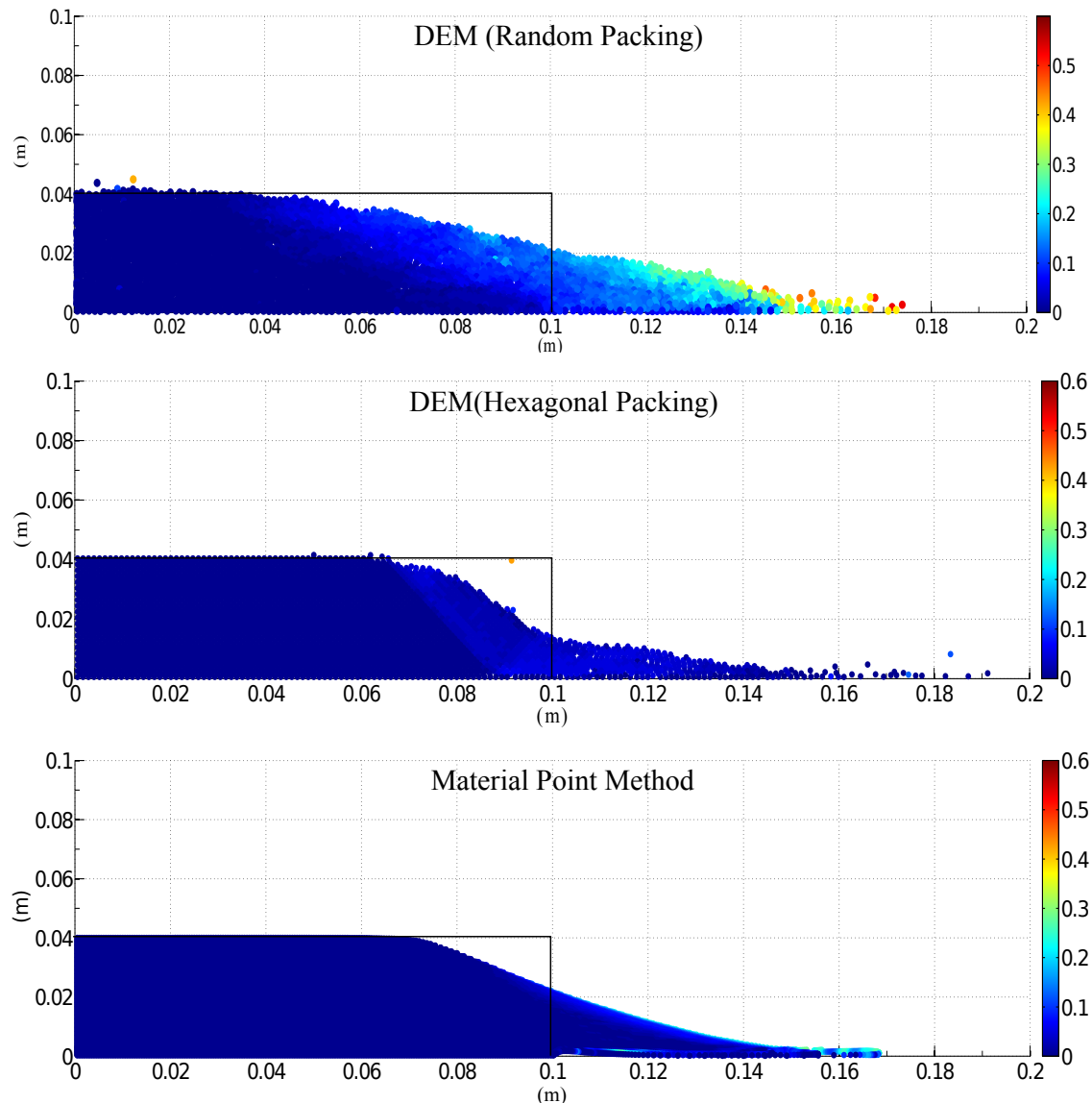


Figure 4.7 Velocity profile of a granular column collapse ($a' = 0.4$ & $t = 3 \times \tau_c$)

For larger aspect ratios, the flow is still initiated by a well defined failure surface as can be seen in figure 4.8. However, in this case the initial granular column is much higher than the top of the failure surface. Due to gravity most of the grains in the column fall in the vertical direction consuming the column along their way. When they reach the vicinity of the failure surface, the flow gets deviated along the horizontal direction releasing a huge amount of kinetic energy gained during the free fall. For larger aspect ratio ($a > 0.7$), the resulting static region is a cone, the final height of the cone, i.e., H_f lies above the summit of the failure surface. Hence, a different evolution is observed from that of the axis-symmetric geometry (Lube et al., 2005), where the final height coincides with the summit of the failure surface forming a truncated conical deposit. Lajeunesse et al. (2004) articulated the variation in the deposit morphology between the axis-symmetric case and the rectangular collapse to be a geometrical effect rather than as an experimental artefact. The final profile of the collapsed granular column with an initial aspect ratio of 6 is presented in Figure 4.9. An initial failure surface starting from the toe end of the column at an angle of about 55° can be observed at critical time τ_c . As the collapse of the granular collapse progresses, successive failure planes parallel to the initial failure surface are formed and shear failure occurs along these planes. The presence of several shear bands in the final profile of the collapsed granular column confirms the hypothesis. crystallisation in hexagonal packing causes a significant effect on the run-out distance by forming series of parallel shear bands. However, the Material Point Method fails to capture the formation of shear bands during the collapse. This observation throws light on the mechanics of propagation of shear bands in massive landslides such as the Storegga submarine landslide. The flow behaviour becomes similar to that of columns with lower aspect ratio as the flow starts descending along the failure plane. Regardless of the experimental configuration and the initial aspect ratio of the columns, the flow is initiated by a well-defined rupture surface, above which the material slides down leaving a static region underneath the failure plane. Depending on the aspect ratio of the column, two asymptotic behaviours are observed. For smaller aspect ratios, the flow is dominated by friction and by the pressure gradient for larger aspect ratio.

To study the flow dynamics of granular columns with different aspect ratios, the flow front $L(t)$ and the maximum height of column $H(t)$ are tracked. The evolution of scaled height (H_f/L_i) and the run-out distance $(L_f - L_i)/L_i$ with time for granular columns with an initial aspect ratio of 0.4 and 6 are presented in Figures. figure 4.10a and figure 4.10b. Time is scaled with respect to the critical time τ_c , defined as the time at which the flow is fully mobilized. Three distinct regions can be observed in the flow evolution of granular column collapse regardless of the initial aspect ratio of the column. An initial transient acceleration phase is observed for a time $0.8\tau_c$. This phase is followed by a heap movement of granular materials at the foot with a constant spreading velocity V for about $2\tau_c$. When time ‘ t ’ > τ_c , the velocity

1 varies linearly with depth in the flowing layer and decreases exponentially with depth near
2 the static layer. This velocity profile is similar to those observed in steady granular surface
3 flows ([Lajeunesse et al., 2004](#)). Most of the run-out happens during this phase. The final phase
4 involves deceleration of the flow front and the flow comes to rest after $0.6\tau_c$. The spreading
5 of the granular column ceases after a time in the order of $3\tau_c$ for all values of aspect ratios,
6 however some motion still persists along the free surface behind the flow front for a much
7 longer time due to internal rearrangement, the duration of which can last up to $t \approx 6\tau_c$. For
8 smaller aspect ratios, the critical time is evaluated as the point of intersection of the scaled
9 run-out and height. The critical time predicted for both hexagonal and random packing of grains
10 matches the experimental observations. However, the Material Point Method overestimates
11 the critical time by a factor of 1.25, which means that it takes longer for the flow to be fully
12 mobilized. However, the actual run-out duration is short and the granular materials comes
13 to rest abruptly at about $t = 3\tau_c$. For columns with larger aspect ratios, the continuum and
14 particulate approaches simulate similar flow evolution behaviour for times up to $3\tau_c$, beyond
15 which particulate simulations stabilise and come to rest, while the flow continues to evolve in
16 MPM simulations resulting in larger run-outs than expected. The flow tends to come to rest at
17 time $t = 6\tau_c$. The three phases in a granular flow can be distinctly observed in the flow evolution
18 plot for a granular column with initial aspect ratio of 6 (see Figure [figure 4.10b](#)). For larger
19 aspect ratios, the flow evolution behaviour observed in the case of random packing matches
20 the experimental observation by [Lajeunesse et al. \(2004\)](#). Hexagonal packing predicts longer
21 time for the flow to evolve, which can be attributed to the increase in the internal resistance
22 due to crystallisation of grains. MPM overestimates the critical time by 50%, however has the
23 same value of run-out as the particulate simulations, at time $t = 3\tau_c$, beyond which the material
24 continues to flow until it ceases at $6\tau_c$. In order to understand the flow dynamics in the case of
25 Material Point Method it is important to study the effect of different parameters on the deposit
26 morphology.

27 **4.2.4 Energy dissipation mechanism**

28 The time evolution of the flow exhibited three distinct stages during the collapse of a granular
29 column. Studying the energy dissipation mechanism provides useful insight into the flow
30 dynamics. shows the time evolution of potential energy (E_p) and kinetic energy (E_k) normalized

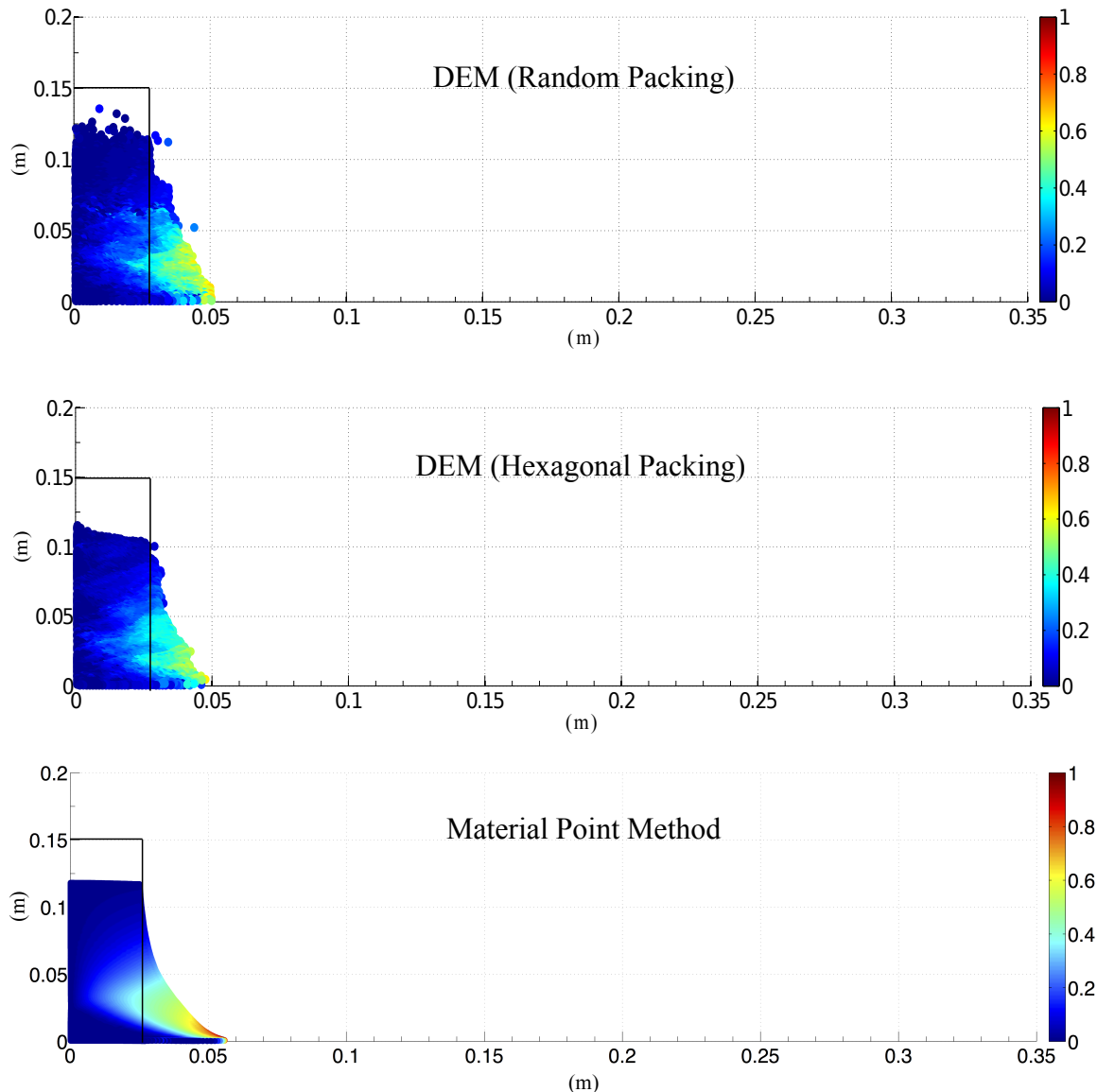


Figure 4.8 Velocity profile of a granular column collapse ($a' = 6$ & $t = \tau_c$)

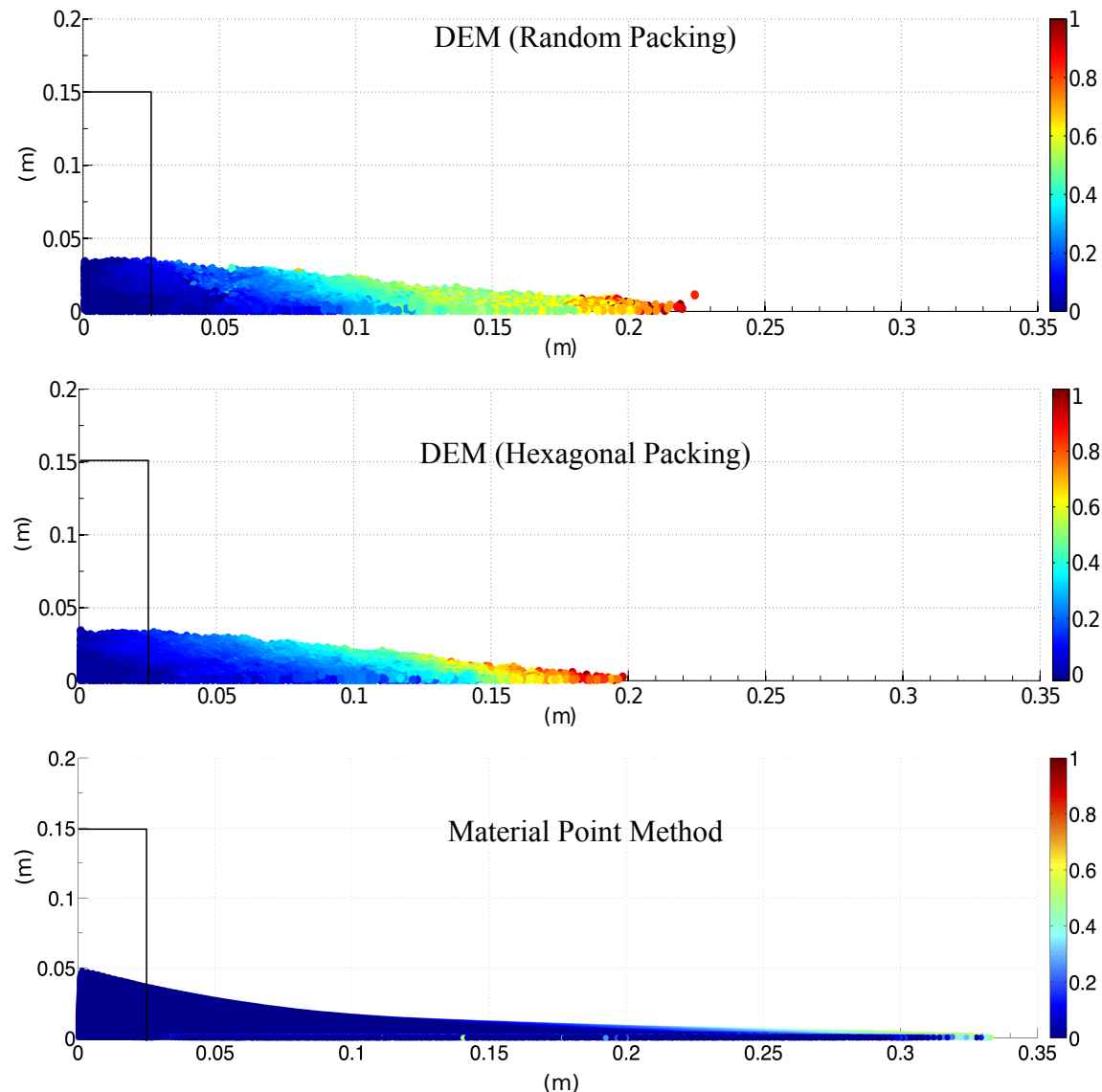


Figure 4.9 Velocity profile of a granular column collapse ($a' = 6$ & $t = 3 \times \tau_c$)

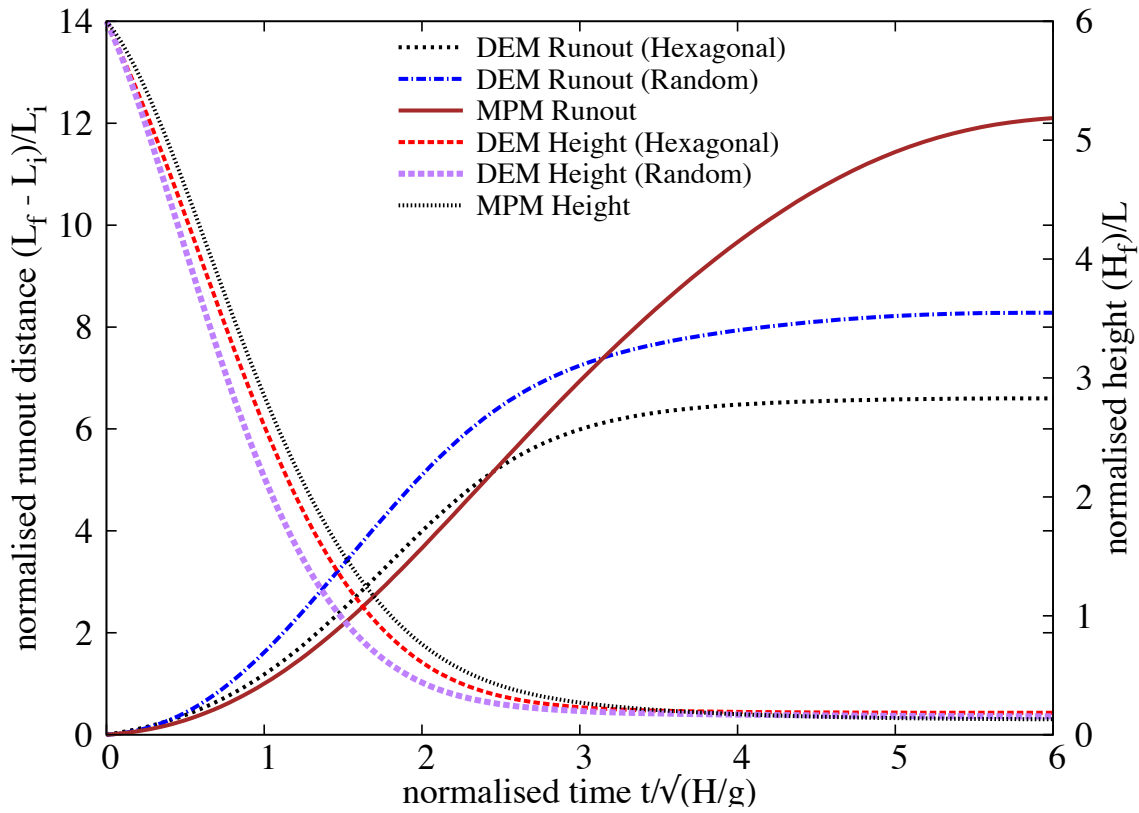
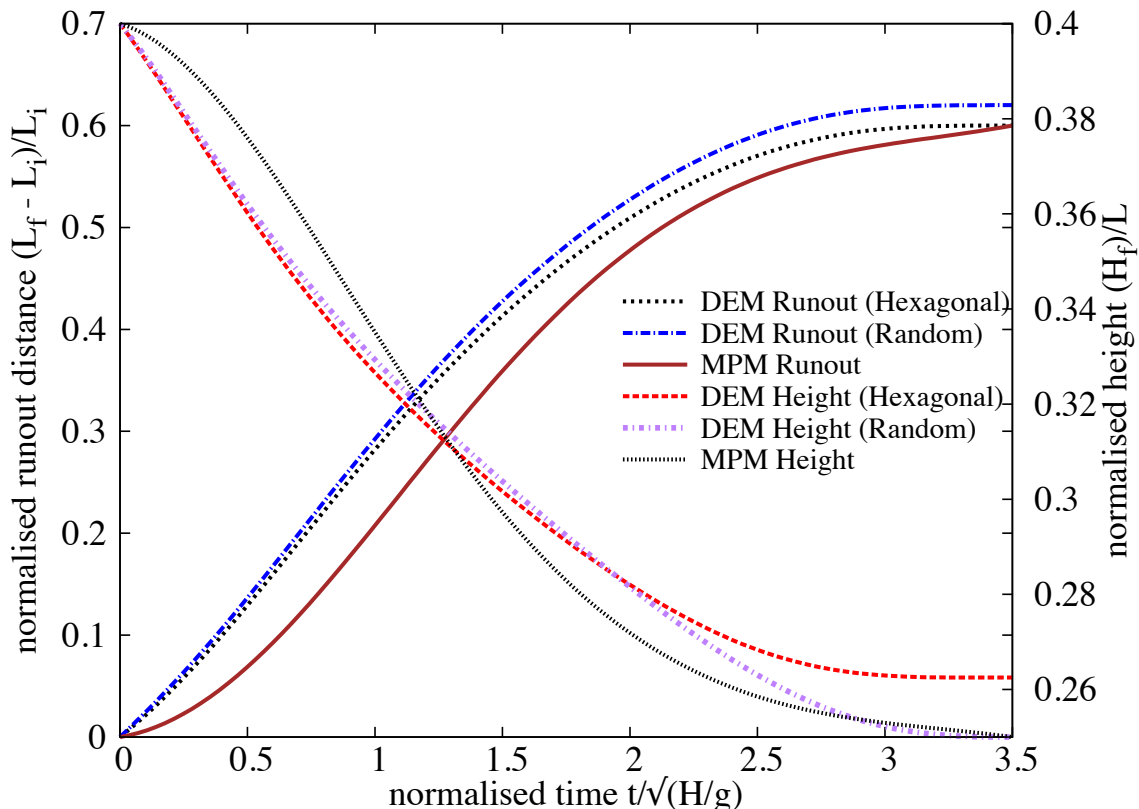


Figure 4.10 Flow evolution of granular column collapse

1 by the initial potential energy E_o .

$$2 \quad E_p = \sum_{p=1}^{N_p} m_p g h_p \quad (4.8)$$

$$3 \quad E_{ki} = \frac{1}{2} \sum_{p=1}^{N_p} m_p v_p^2 \quad (4.9)$$

4 where N_p is the total number of particles, m_p is the mass of a particle ‘ p ’, h_p is the height and
 5 v_p is the velocity of the particle ‘ p ’. It can be observed from the figure that the initial potential
 6 energy stored in the particle is converted to kinetic energy which is dissipated as the granular
 7 material flows down. Three successive stages can be identified in the granular column collapse.
 8 In the initial acceleration stage ($t < 0.8\tau_c$), the initial potential energy stored in the grains is
 9 converted into vertical motion. In the second stage, the grains undergo collisions with the
 10 bottom plane and/or with neighbouring grains, and the stored potential energy is converted into
 11 horizontal motion. In the third stage, the grains eventually leave the base area of the column
 12 and flow sideways. As the process involves collective dynamics of all the particles, it is difficult
 13 to predict the exact trajectory of a grain, however, the overall dynamics can be explained. To
 14 explain the dissipation of energy during the collapse, [Staron et al. \(2005\)](#) assumed that the total
 15 initial potential energy stored in the system is completely dissipated through friction over the
 16 entire run-out distance as:

$$18 \quad \mu m_o g \times (L_f - L_i) = m_o g H_o \quad (4.10)$$

20 where μ is the friction coefficient. The model predicts well the flow dynamics for columns
 21 with larger aspect ratios, as most of the initial potential energy is dissipated during the collapse
 22 involving the entire column. However, for columns with smaller aspect ratios, only a portion of
 23 the mass above the failure surface is involved in the flow. Hence, the energy dissipation should
 24 involve only the grains lying above the failure surface. A mathematical model, which considers
 25 the grains lying above the failure surface, will be derived to predict the flow dynamics of the
 26 granular column collapse for different aspect ratios.

27 4.2.5 Role of initial grain properties

28 It should be noted that the collapse experiment is highly transient and no clear stationary regime
 29 was observed. On the contrary, the acceleration and the deceleration phases cover nearly the
 30 whole duration of the spreading. This makes the analysis of the structure of the flow and its
 31 relation with other characteristic of the system uneasy. Considering this, we were able to show

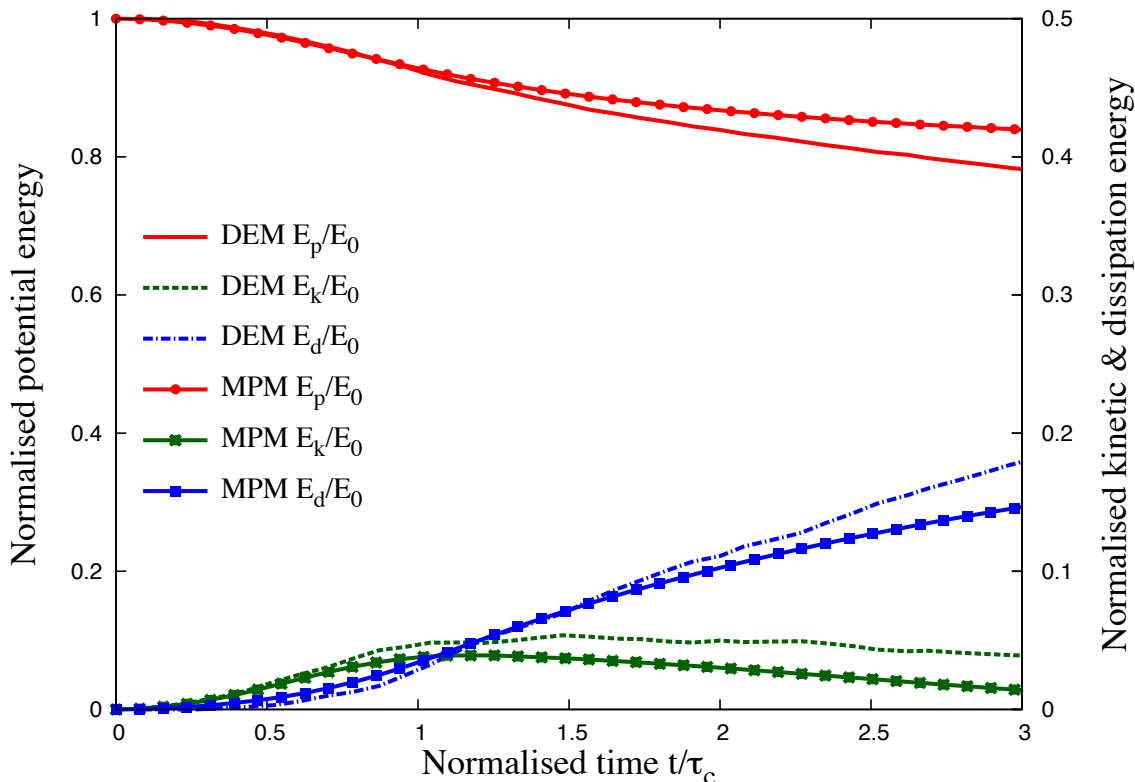
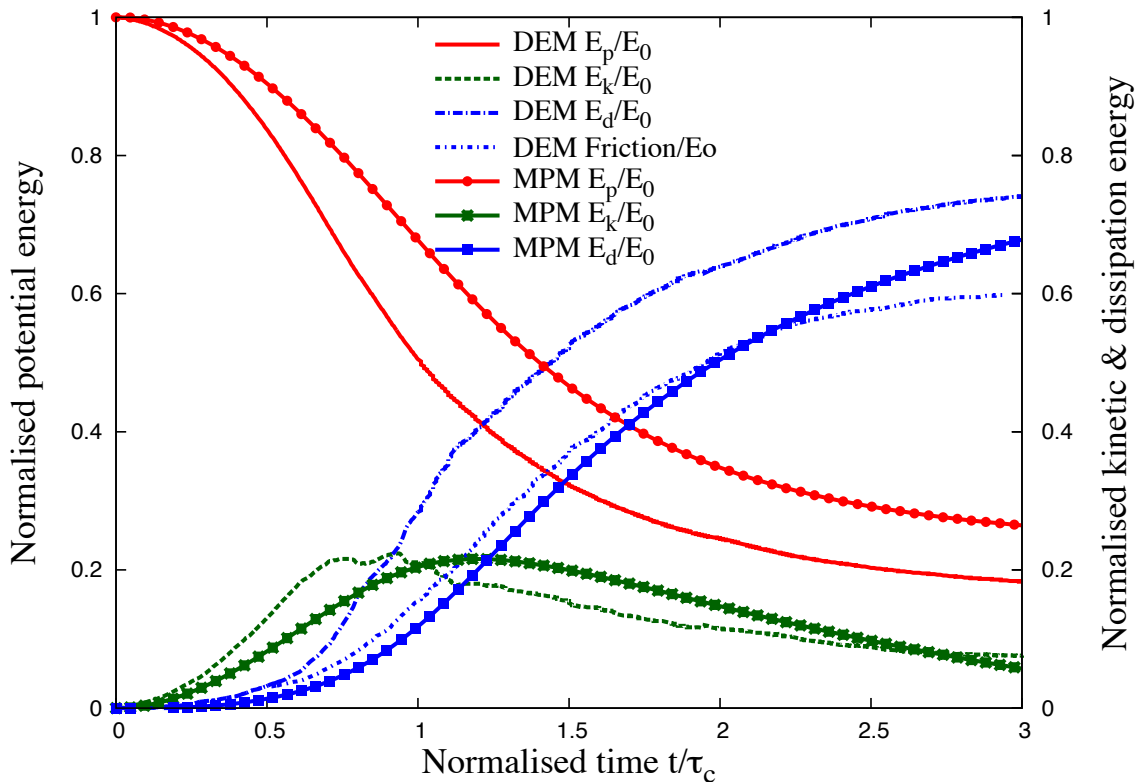
(a) Energy evolution of a column with ' a' = 0.4(b) Energy evolution of a column with ' a' = 6

Figure 4.11 Energy evolution of granular column collapse

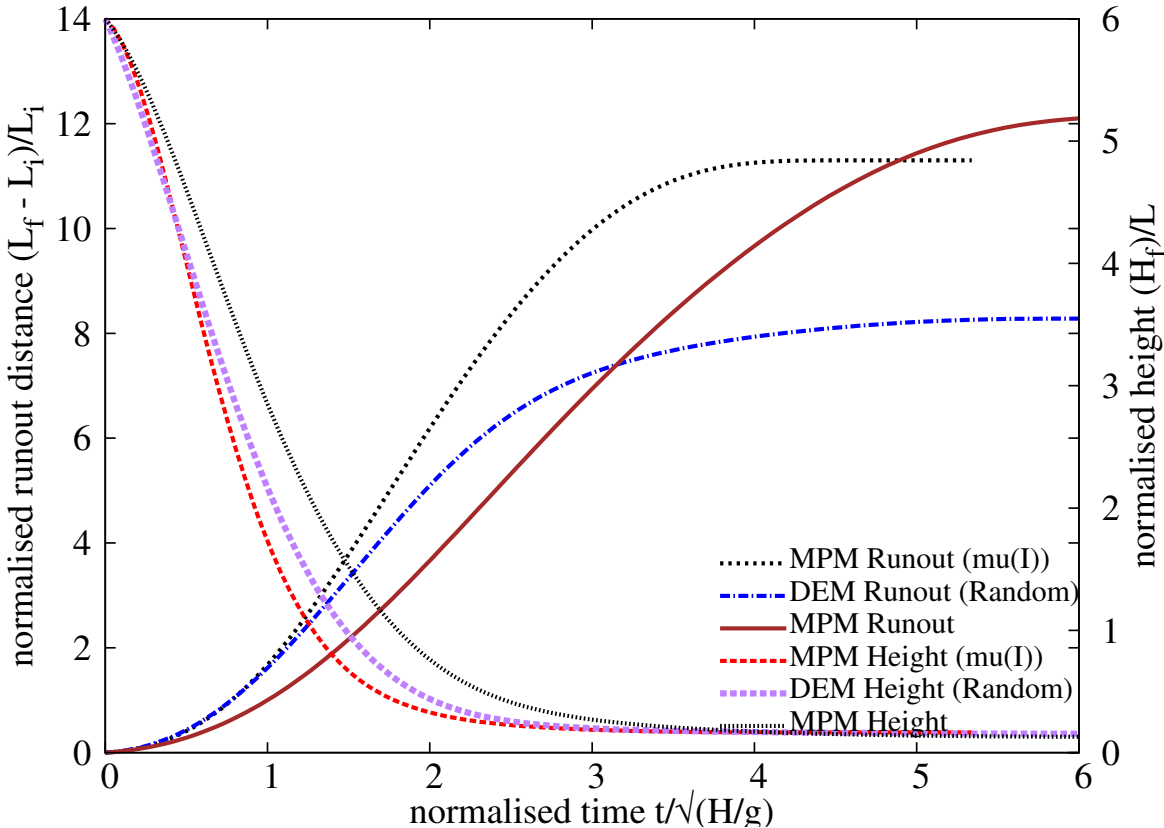
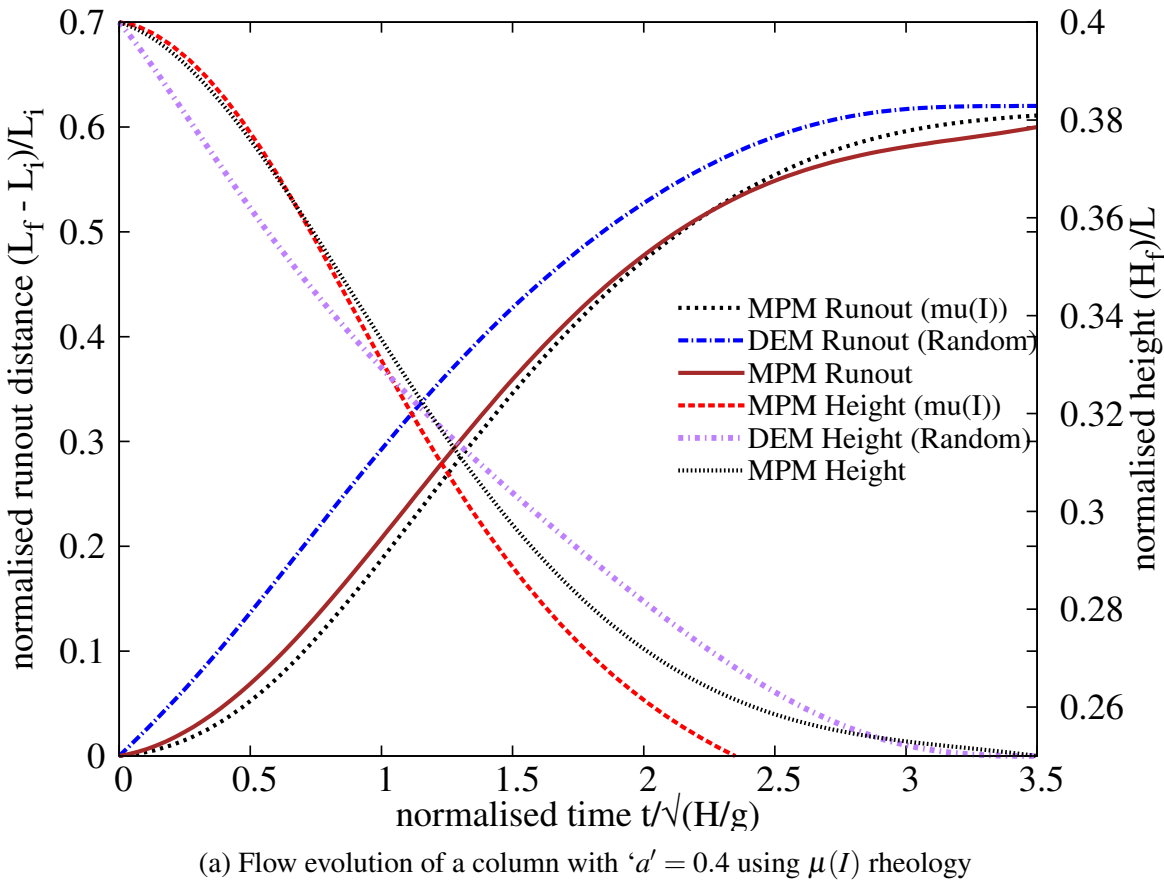


Figure 4.12 Flow evolution of granular column collapse using $\mu(I)$ rheology

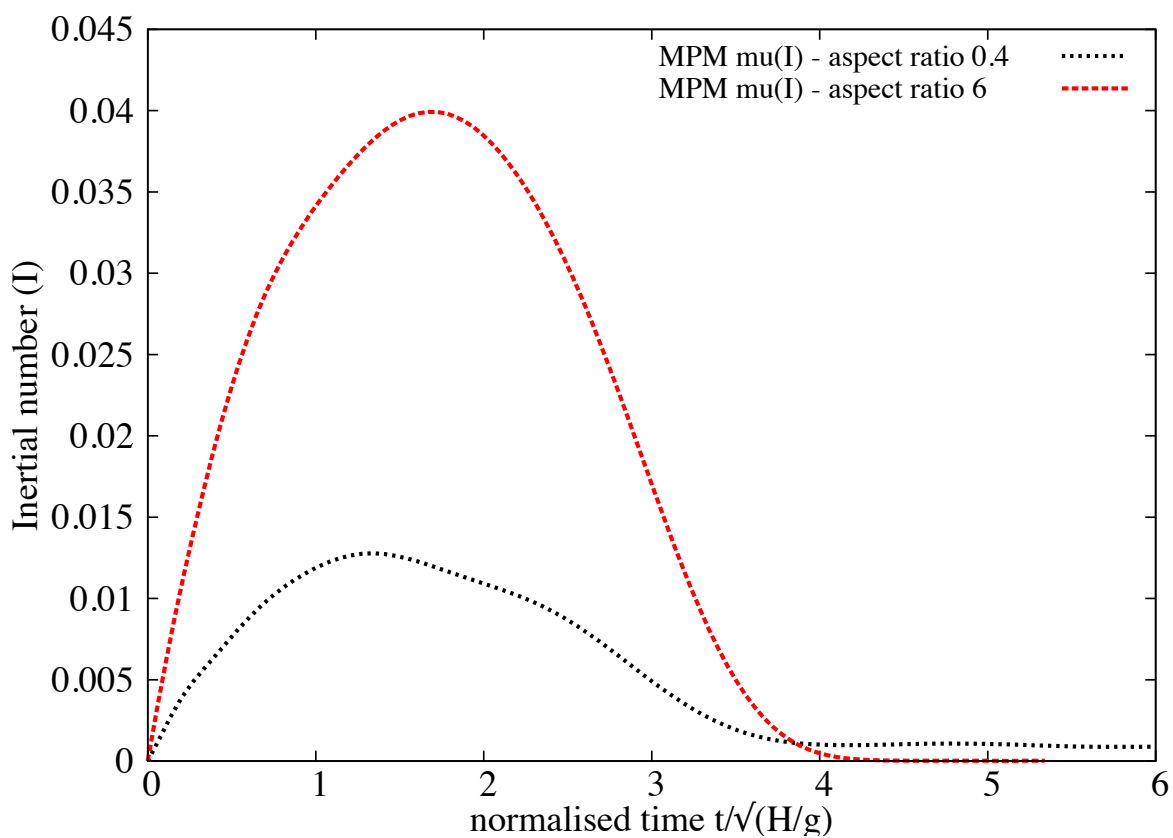


Figure 4.13 Evolution of inertial number with time for columns with ' $a' = 0.4$ and ' $a' = 6$

1 nevertheless how the initial condition was dominating the behaviour of the spreading through
2 the mass distribution induced in the flow. This means that the knowledge of the final run-out is
3 not a sufficient characterization of the deposit: one also needs to know how mass is distributed
4 to understand the dynamics and the dissipation process. This is expected to be true in natural
5 contexts as well as in experiments. While the inter-grain friction μ does not affect the early
6 vertical dynamics, nor the power-law dependence, it controls the effective frictional properties
7 of the flow, and its internal structure. It is interesting to note that the details of the structure of
8 the flow do not influence the final run-out dependence, and thus seem to play a marginal role in
9 the overall behaviour of the spreading. This could explain why simple shallow-water model
10 with basic rheology but where the free-fall dynamics was accounted for could reproduce the
11 run-out scalings.

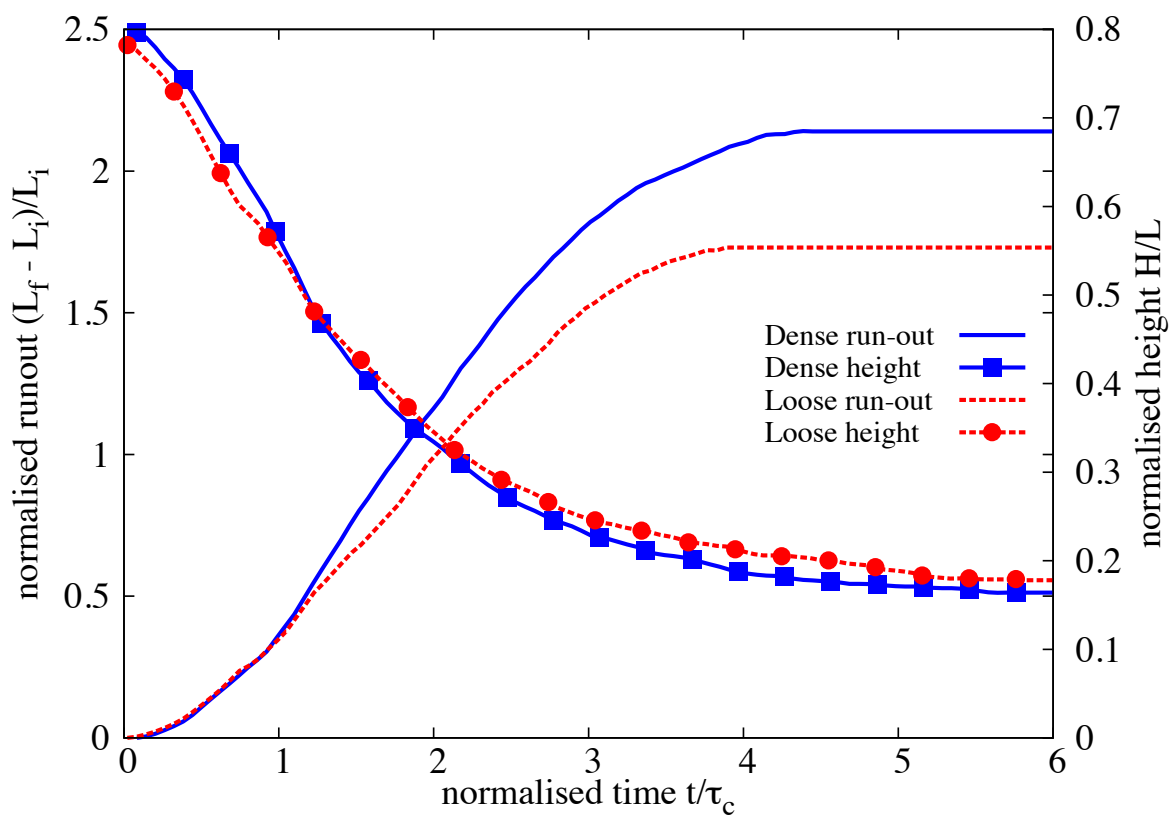
12 At this stage, it appears that the collapse experiment for large aspect ratios mixes two very
13 different dynamics: while the second stage consists of a “conventional” horizontal granular
14 flows, the first stage implies a large vertical acceleration. It shows how the initial condition can
15 influence the overall behaviour of a granular system, and suggests that triggering mechanisms
16 play a crucial role in the case of natural flows. This stresses the necessity of accounting for
17 vertical acceleration in continuum models in the perspective of producing realistic prediction
18 of the behaviour of granular flows.

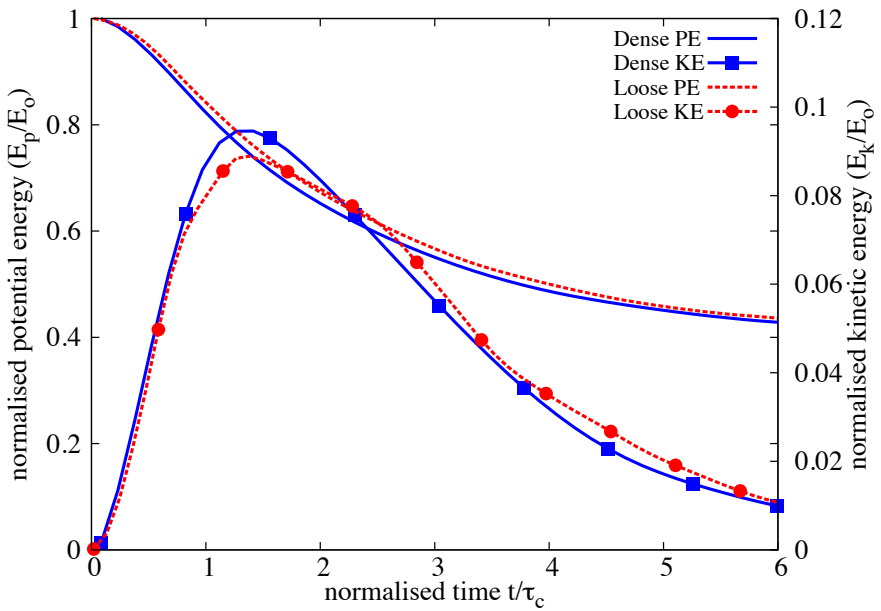
19 The numerical constants of proportionality, however, show clear material dependence. This
20 corroborates the conclusion of [Balmforth and Kerswell \(2005\)](#); [Lajeunesse et al. \(2004\)](#) and
21 softens that of [Lube et al. \(2005\)](#).

22 **4.3 Slopes subjected to impact loading**

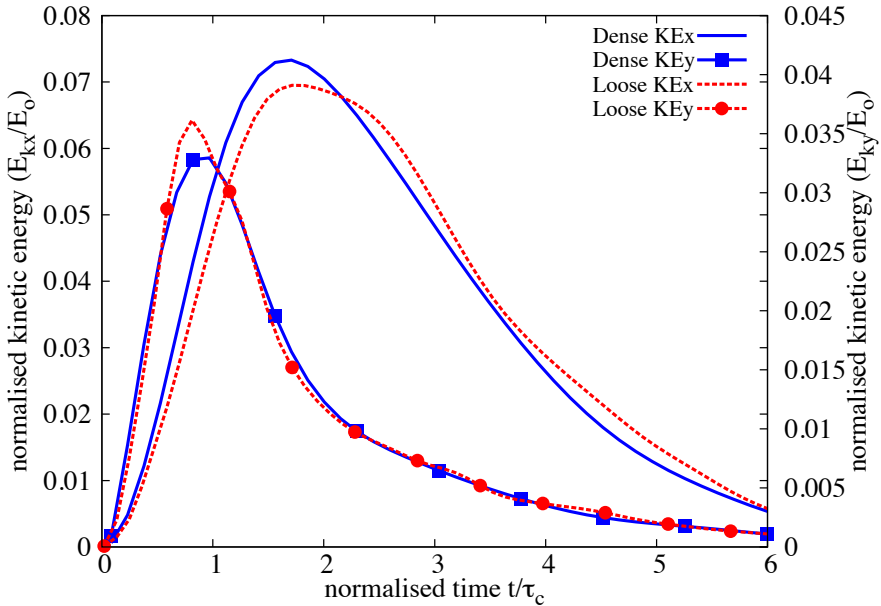
23 Transient granular flows occur very often in nature. Well-known examples are rockfalls, debris
24 flows, and aerial and submarine avalanches. They form a major element of landscape reshape
25 and their high destructive potential is a substantial factor of risk. Natural granular flows may be
26 triggered as a result of different processes such as gradual degradation, induced by weathering
27 or chemical reactions, liquefaction and external forces such as earthquakes.

28 Granular flows have been studied in laboratory experiments in different geometries such as
29 tilted piles leading to slope failure and surface avalanches ([Iverson, 1997](#); ?) or by considering
30 vertical columns of grains collapsing and spreading under their own weight ([Lajeunesse et al.,](#)
[2004, 2005](#)). The dynamics observed in the experiments is often nontrivial in the sense that
32 the final configurations after the dissipation of the whole kinetic energy can not be readily
33 predicted by means of simple laws based on the Mohr-Coulomb nature of the material. For

Figure 4.14 Effect of density on run-out evolution ' a' = 0.8

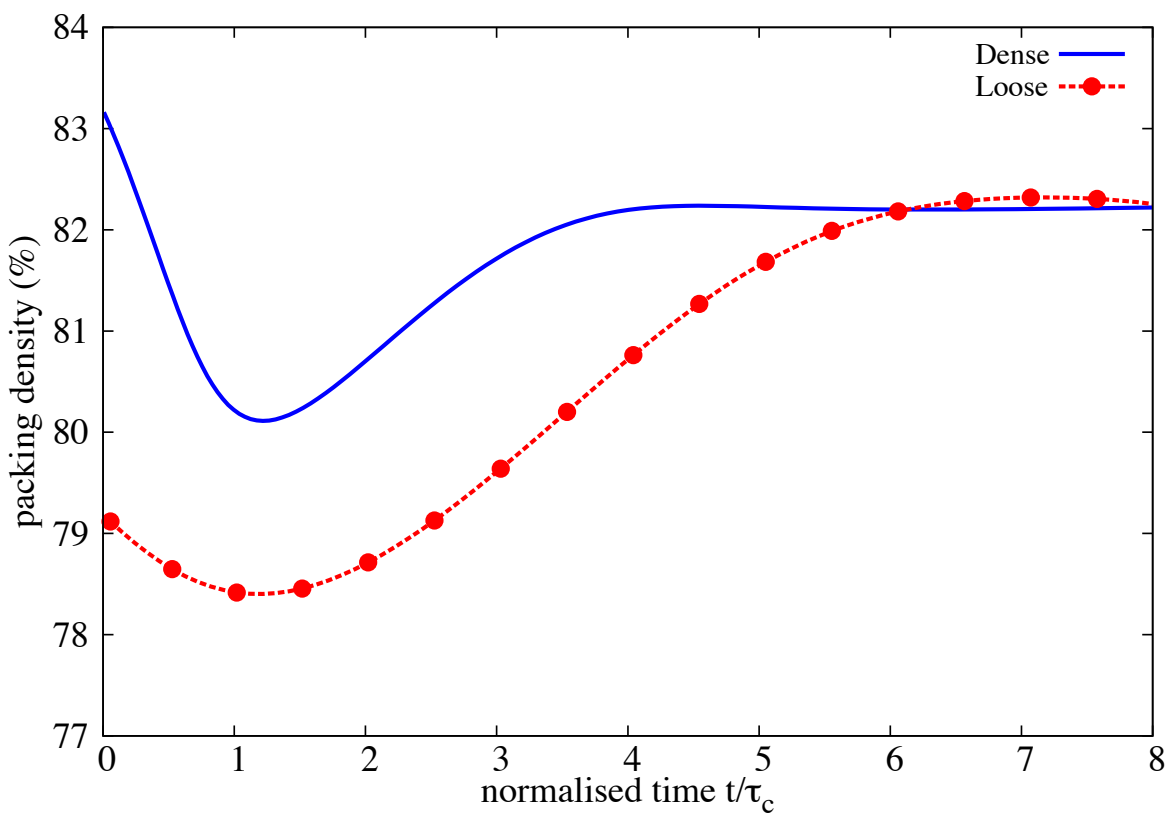


(a) Evolution of potential and kinetic energy



(b) Effect of kinetic energy

Figure 4.15 Effect of density on energy evolution $a = 0.8$

Figure 4.16 Evolution of local packing density ' a' = 0.8

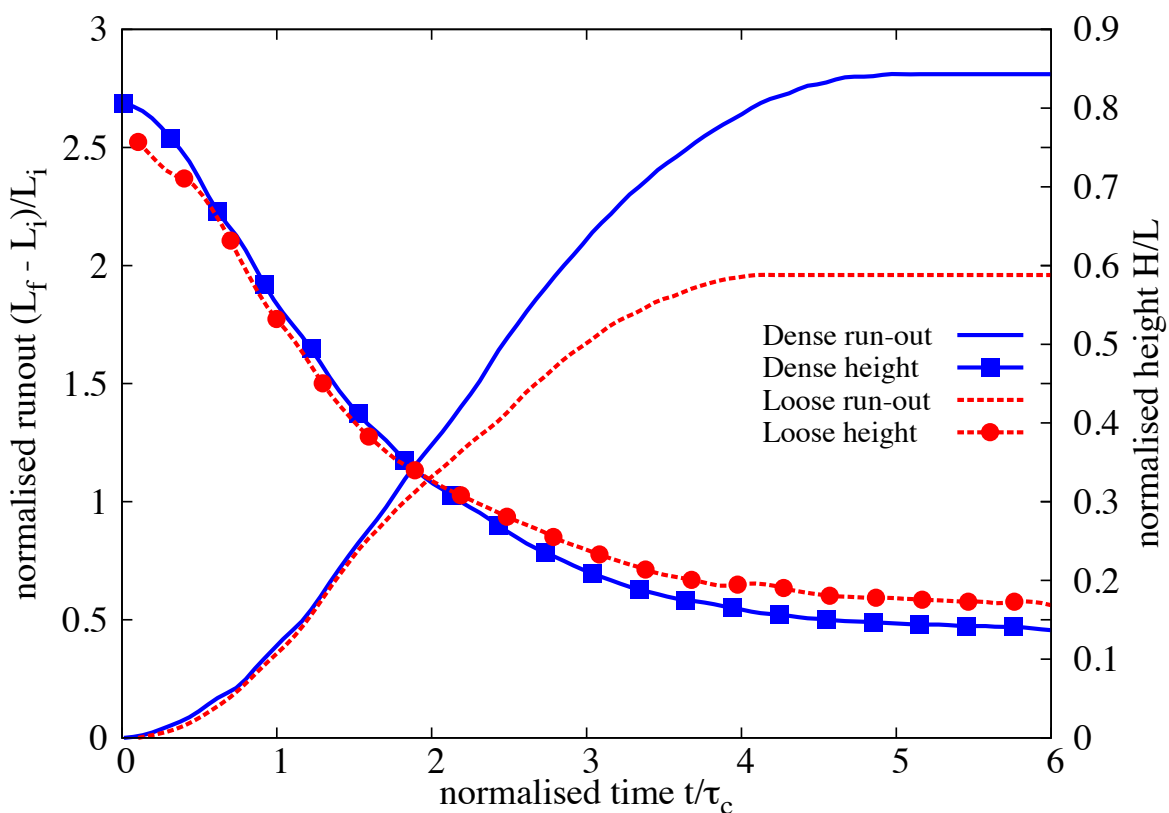


Figure 4.17 Effect of density on run-out evolution ' a' = 0.8 (poly-dispersity ' r ' = 6)

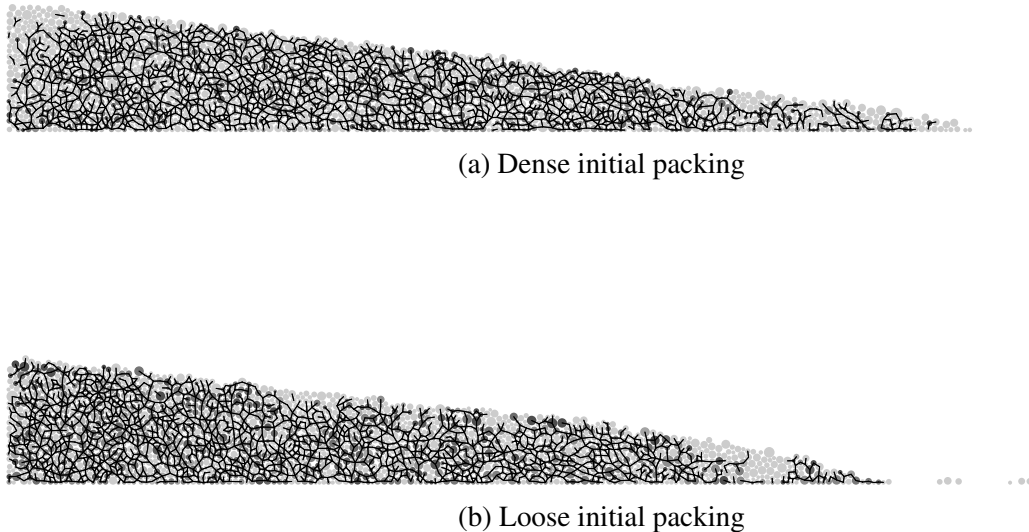
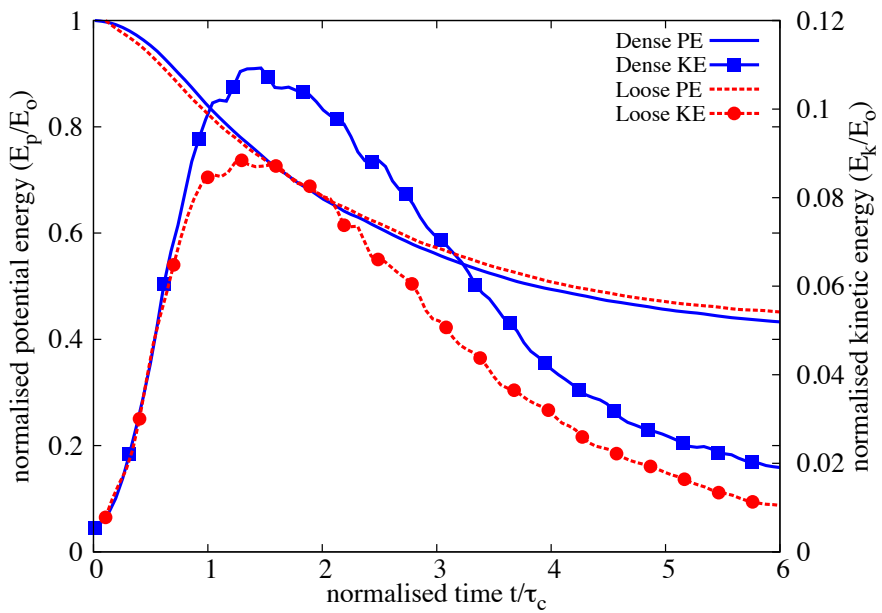


Figure 4.18 Snapshots of granular column collapse $t = 6\tau_c$

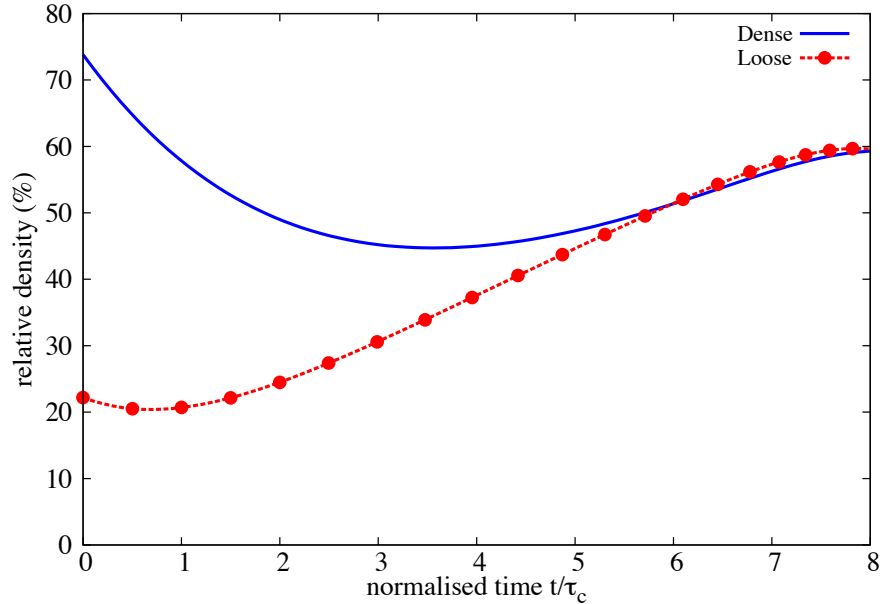
example, in collapsing columns, the run-out distance is found to obey a power-law dependence
upon the initial aspect ratio of the column.

The observed nontrivial transient dynamics is often correctly reproduced by the DEM,
which provides a powerful tool for the grain-scale analysis of the trigger and its subsequent
dynamics (Staron and Lajeunesse, 2009; Staron et al., 2005). However, even in simplified
geometries such as those investigated in the experiments, the DEM suffers from a serious
short-coming in the number of particles that can be simulated in a reasonable time. This is a
critical issue when more complex geometries or long-time granular processes are considered, or
when particle size distributions are broad. For this reason, most numerical studies are performed
in 2D or simple particle shapes and size distributions are considered.

It is also obvious that classical modelling strategies based on the finite element method
(FEM) cannot be used for the simulation of very large deformations. In various applications of
FEM, this problem is treated by means of technical tools such as re-meshing. Such methods are,
however, not robust and lead to round-off errors and mesh-sensitivity. In contrast, the so-called Material Point Method (MPM) is an alternative approach for continuum problems that
allows for indefinitely large deformations without re-meshing ?. In this method, the material
points carry the information on state variables and a background fixed grid is used to solve the
governing equations. The information between the material points and the grid is exchanged
via suitable shape functions. The MPM has been applied with success to a number of solid

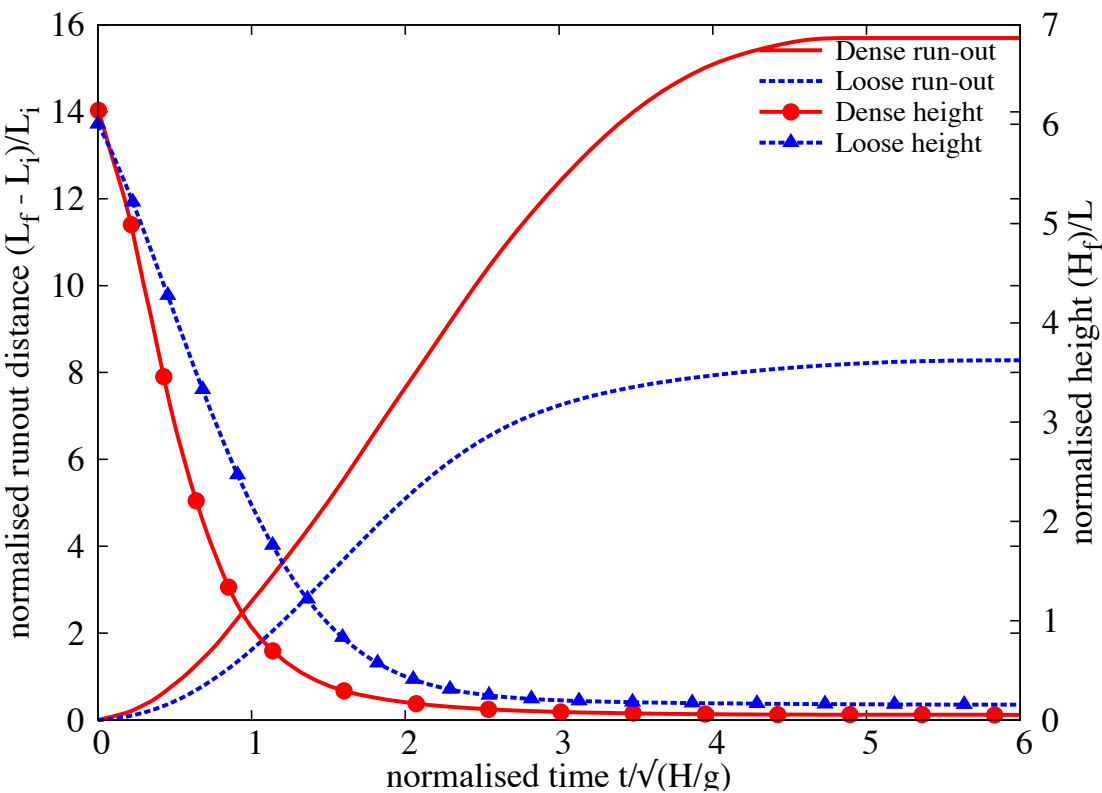


(a) Evolution of potential and kinetic energy

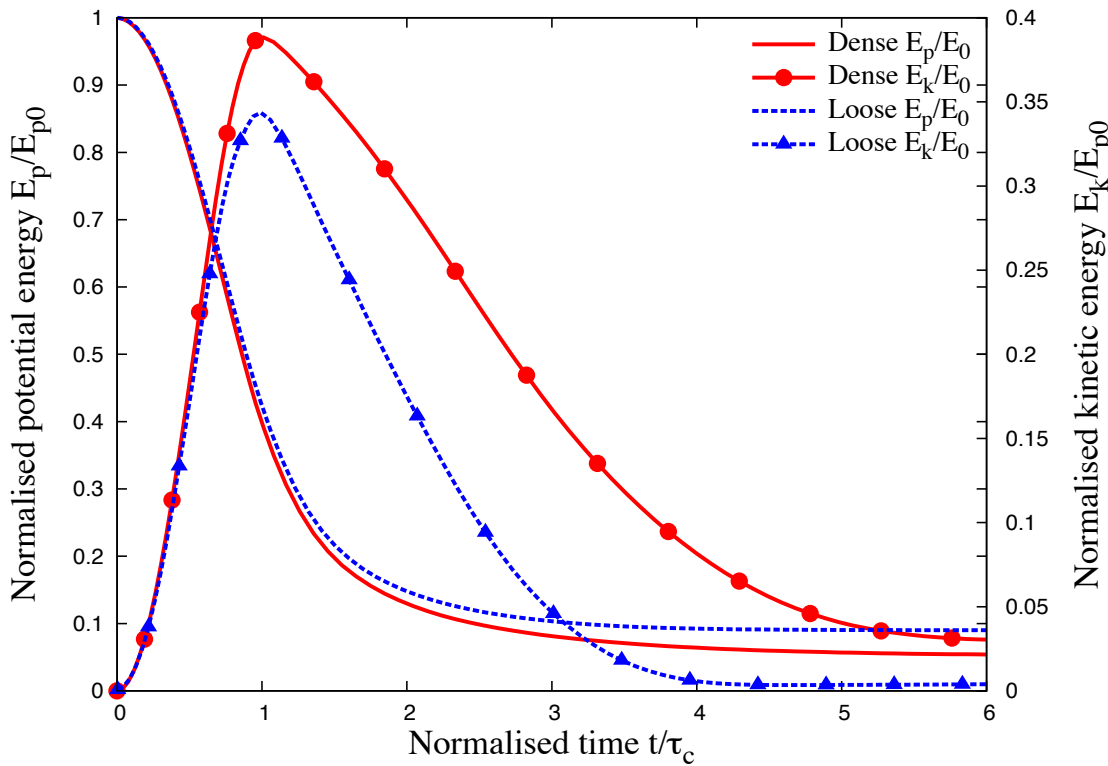


(b) Evolution of packing density

Figure 4.19 Effect of density on energy and packing fraction evolution ' a' = 0.8 (poly-dispersity ' r ' = 6)



(a) Effect of density on run-out evolution



(b) Effect of density on energy evolution

Figure 4.20 Effect of density on run-out behaviour and energy evolution ' a' = 0.6

¹ mechanics problems and its theoretical foundations have recently been investigated by several
² authors.

³ In this paper, we are concerned with the ability of the MPM, as a continuum approach,
⁴ to reproduce the evolution of a granular pile under its own weight or when destabilized by
⁵ energy input. In particular, a central issue is whether power-law dependence of the run-out
⁶ distance and time with respect to the initial geometry or energy can be reproduced by a simple
⁷ prescription of the Mohr-Coulomb plastic behaviour within a MPM code. We therefore perform
⁸ extensive simulations by varying continuously different input parameters and compare the data
⁹ with those obtained from DEM simulations of the same system. We compare in detail the
¹⁰ evolution of the profile of the pile and its total kinetic energy between the two methods and
¹¹ for different initial states. As we shall see, the MPM can successfully simulate the transient
¹² evolution with a single input parameter, namely the internal angle of friction. This opens the
¹³ way to the simulation of geological-scale flows on complex topographies.

¹⁴ 4.3.1 Numerical procedures

¹⁵ The numerical samples are composed of ~ 13000 disks with a uniform distribution of diameters
¹⁶ by volume fractions in the range $[d_{min}, d_{max}]$ with $d_{max} = 1.5d_{min}$. The mean particle diameter
¹⁷ and mass are $d \simeq 0.0025$ m and $m \simeq 0.0123$ kg, respectively. The particles are first poured
¹⁸ uniformly into a rectangular box of given width and then the right-hand side wall is shifted
¹⁹ further to the right to allow the particles to spread. A half-pile is obtained when all particles
²⁰ come to rest; see Fig. ???. This procedure leads to a mean packing fraction $\simeq 0.83$.

Table 4.4 DEM simulation of simple shear test (?)

Parameter	Value
Mean grain diameter	≈ 2.455 mm
Grain diameter $[d_{min} : d_{max}]$	[2.0, 3.0] mm
Friction coefficient	0.4
Grain density	2600kg m^{-3}
Restitution coefficient	0
Number of grains	1174

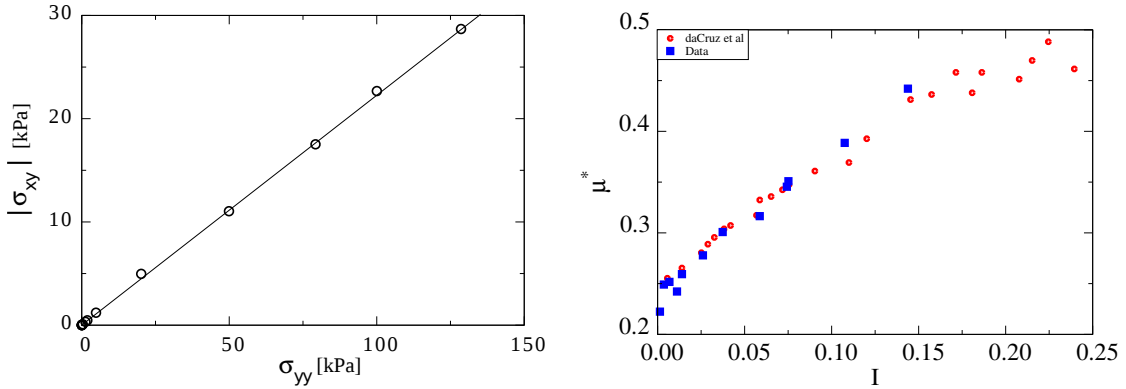
²¹ The initial static pile is set into motion by applying a constant horizontal gradient $v_{0x}(y) =$
²² $k(y_{max} - y)$ with $k > 0$. Such a configuration mimics the energy transfer mechanism of a
²³ horizontal quake along the bottom of the pile. We are interested in the evolution of the
²⁴ geometry of the pile and its total kinetic energy as a function of the initial input energy E_0 . The
²⁵ run-out distance R_f is the distance of the rightmost particles from the left wall when the pile

comes to rest. It will be normalized by the initial extension R_0 of the pile, as in the experiments of collapsing columns. The total run-out duration t_f is the time that the pile takes to reach its final run-out distance R_f .

The initial static pile is set into motion by applying a horizontal velocity $v_{0x}(y)$ to all particles during a short interval of time. Different velocity fields were tested: 1) The same velocity $v_{0x}(y) = v_0$ applied to all particles, 2) The same velocity $v_{0x}(y) = v_0$ applied to a column of particles next to the left wall, 3) a constant velocity gradient $v_{0x}(y) = k(y_{max} - y)$ with $k > 0$. The first two pushing modes mimic the case of a pile impacted from the left by a moving mass (tsunami, debris...) whereas the last mode represents energy transfer by horizontal quake of the bottom line. We will compare briefly below the effect of different pushing modes, but later we will mainly explore the third mode. We are interested in the evolution of the geometry of the pile and its total kinetic energy as a function of the initial energy input E_0 . The run-out distance R_f is the distance of the rightmost particles from the left wall when the pile comes to rest. It will be normalized by the initial extension R_0 of the pile, as in the experiments of collapsing columns. The total run-out duration t_f is the time that the pile takes to reach its final run-out distance R_f .

For grain scale simulations, classical DEM and Contact Dynamics approach is used. A detailed description of the Contact Dynamics method can be found in [Jean \(1999\)](#); [Radjai and Dubois \(2011\)](#); [Radjai and Richefeu \(2009\)](#); ?. This method is based on implicit time integration of the equations of motion and a nonsmooth formulation of mutual exclusion and dry friction between particles. The CD method requires no elastic repulsive potential and no smoothing of the Coulomb friction law for the determination of forces. For this reason, the simulations can be performed with large time steps compared to discrete element simulations. The unknown variables are particle velocities and contact forces, which are calculated at each time step by taking into account the conservation of momenta and the constraints due to mutual exclusion between particles and the Coulomb friction. We use an iterative research algorithm based on a nonlinear Gauss-Seidel scheme. The only contact parameters within the CD method are the friction coefficient μ_s , the normal restitution coefficient e_n and the tangential restitution coefficient e_t between particles. We will investigate the effect of these parameters on the evolution of kinetic energy and the profile of the pile.

The natural units of our system are the mean particle diameter d , mean particle mass m and gravity g . For this reason, in the following we normalize the lengths by d , the times by $(d/g)^{1/2}$, the velocities by $(gd)^{1/2}$ and the energies by mgd .



(a) Evaluating the critical state friction angle from periodic shear test.
(b) Evolution of Inertial number with friction μ

Figure 4.21 Periodic shear test using CD (?).

4.3.2 Evolution of pile geometry and run-out

In this section, we consider the spreading process following the initial energy input into the pile. Fig. ?? shows several snapshots of the pile for an initial input energy $E_0 = 61$ (in dimensionless units). The pile is sheared from the bottom to the top, thus leaving a cavity in the vicinity of the left wall. The cavity is partially filled while the pile continues to spread to the right.

In this section, we consider the spreading process following the initial energy input into the pile. Fig. ?? shows several snapshots of the pile for each pushing mode and for the same initial energy $E_0 = 61$ (in dimensionless units). In mode 1, where the same velocity is imparted to all particles, the whole pile moves away from the left wall over a short distance and then it spreads out and declines in slope. The spreading continues farther until the slope nearly declines to zero. In mode 2, where the velocity is applied to a column of particles next to the left wall, the particles belonging to the column are literally expelled from the pile. They fall back farther way on the pile after a ballistic travel above the pile. At the same time, the right side of the pile slightly spreads away while the left side is filled by the particles rolling down into the gap left by the column. In mode 3, the pile is sheared from the bottom to the top, leaving thus a cavity in the vicinity of the left wall. The cavity is partially filled while the pile continues to spread.

All pushing modes involve a transient with a sharp change of the geometry of the pile followed by continuous spreading to the right. In mode 2, most of the energy is carried away by the ejected particles. In mode 1, the pile has a rigid-body velocity component and moves away from the left wall, but shows an efficient energy transfer leading to a long run-out distance. The transient is more energy consuming in mode 3 compared to mode 1. For this reason, the run-out distance in mode 3 is long but shorter than in mode 1. In the following, we analyze in more detail the evolution of the pile in mode 3, which mimics a horizontal quake from the bottom

and, despite the creation of a cavity, remains always in contact with the left wall irrespective of the input energy.

Figure 4.4 shows the normalized run-out distance $(R_f - R_0)/R_0$ and total run-out time t_f as a function of the input energy E_0 . We observe two regimes both characterized by a power-law run-out distance and time as a function of E_0 . In the first regime, corresponding to the range of low input energies $E_0 < 40 \text{ mgd}$, the run-out distance varies as $R_f \propto (E_0)^\alpha$ with $\alpha \simeq 0.61 \pm 0.04$ over nearly one decade while the duration keeps a constant value $t_f \simeq 60 (d/g)^{0.5}$ irrespective of the value of E_0 ! The error on the value of the exponent represents the confidence interval of linear fits on the logarithmic scale. An average run-out speed can be defined from the ratio $v_s = (R_f - R_0)/t_f$. According to the data, we have $v_s \propto (E_0)^{0.61 \pm 0.04}$. Since the initial average velocity varies as $v_0 \propto (E_0)^{0.5}$, this difference between the values of the exponents suggests that the mobilized mass during run-out declines when the input energy is increased. As we shall see below, the constant run-out time reflects also the collapse of the particles into the cavity left behind the pile.

In the second regime, corresponding to the range of high input energies $E_0 > 40 \text{ mgd}$, the run-out distance varies as $R_f \propto (E_0)^{\alpha'}$ over one decade with $\alpha' \simeq 0.77 \pm 0.03$ while the duration increases as $t_f \propto (E_0)^{\beta'}$ with $\beta' \simeq 0.21 \pm 0.04$. Hence, in this regime the average run-out speed varies as $v_s \propto (E_0)^{0.56 \pm 0.07}$. This exponent is close to the value 0.5 in $v_0 \propto (E_0)^{0.5}$, and hence, within the confidence interval of the exponents, in the second regime we may assume $\beta' \simeq \alpha' - 0.5$ and $v_s \propto v_0$.

It is worth noting that a similar power-law dependence of the run-out distance and time were found in the case of collapsing columns of grains with respect to the initial aspect ratio Topin et al. (2012). In the column geometry, the particles spread away owing to the kinetic energy acquired during gravitational collapse of the column. Topin et al. found that the run-out distance varies as a power law of the available peak kinetic energy at the end of the free-fall stage with an exponent $\simeq 0.5$. This value is below those obtained here for both regimes. This is, however, physically plausible since the distribution of particle kinetic energies at the end of the collapse is more chaotic than in our simulations where the energy is supplied from the very beginning in a well-defined shear mode. As pointed out by Staron et al. (2005), the distribution of kinetic energies is an essential factor for the run-out distance.

4.3.3 Decay of kinetic energy

The non-trivial evolution of the pile geometry in two regimes suggests that the energy supplied to the pile is not simply dissipated by shear and friction with the bottom plane. We also need to split the kinetic energy into its different components (x , y and rotation) of the velocity field. The input energy is in the x component, but due to both the creation of a cavity next to the left

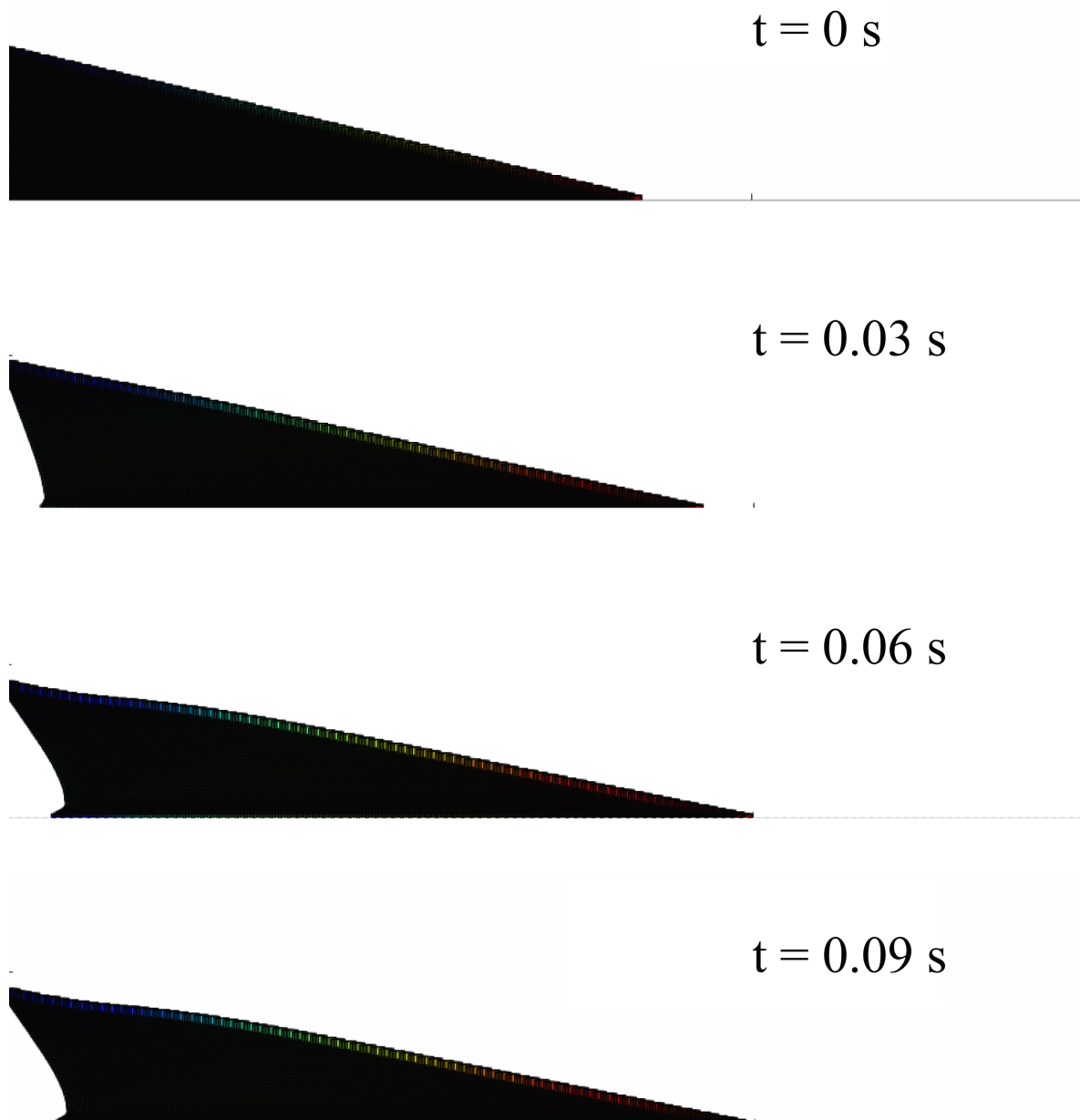


Figure 4.22 Snapshots of MPM simulations of the evolution of granular pile subjected to a gradient impact energy.

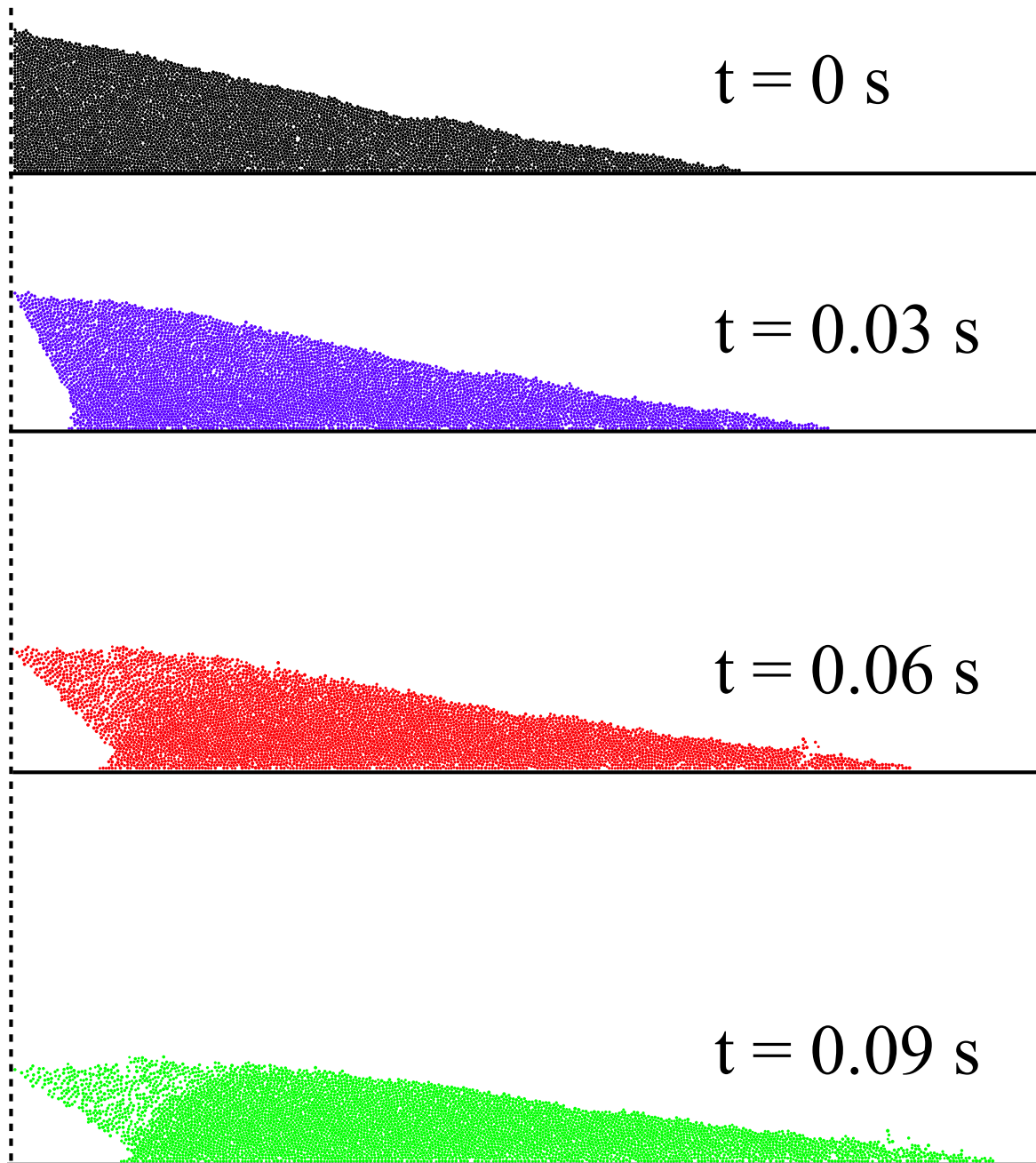


Figure 4.23 Snapshots of CD simulations of the evolution of granular pile subjected to a gradient impact energy (?).

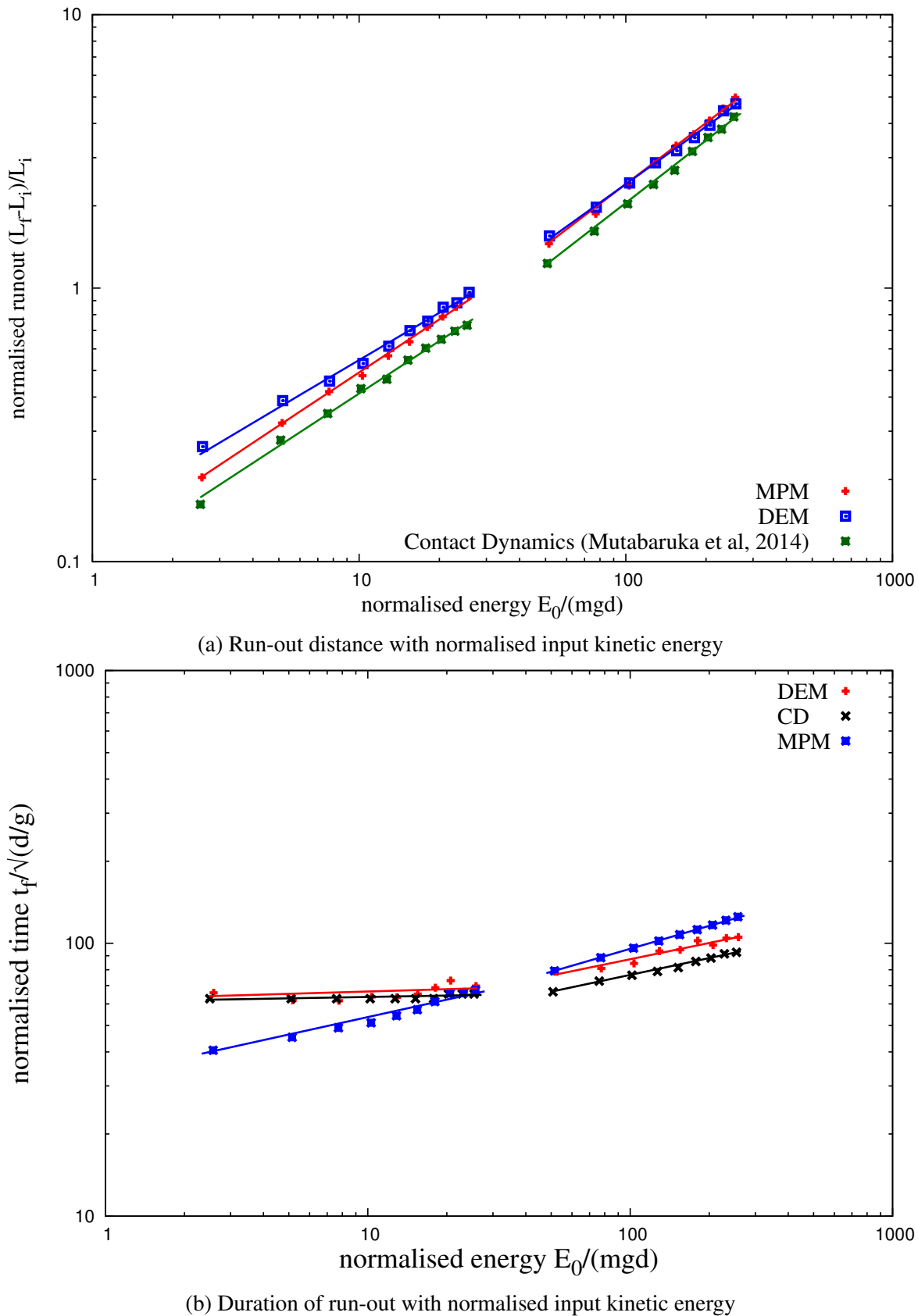


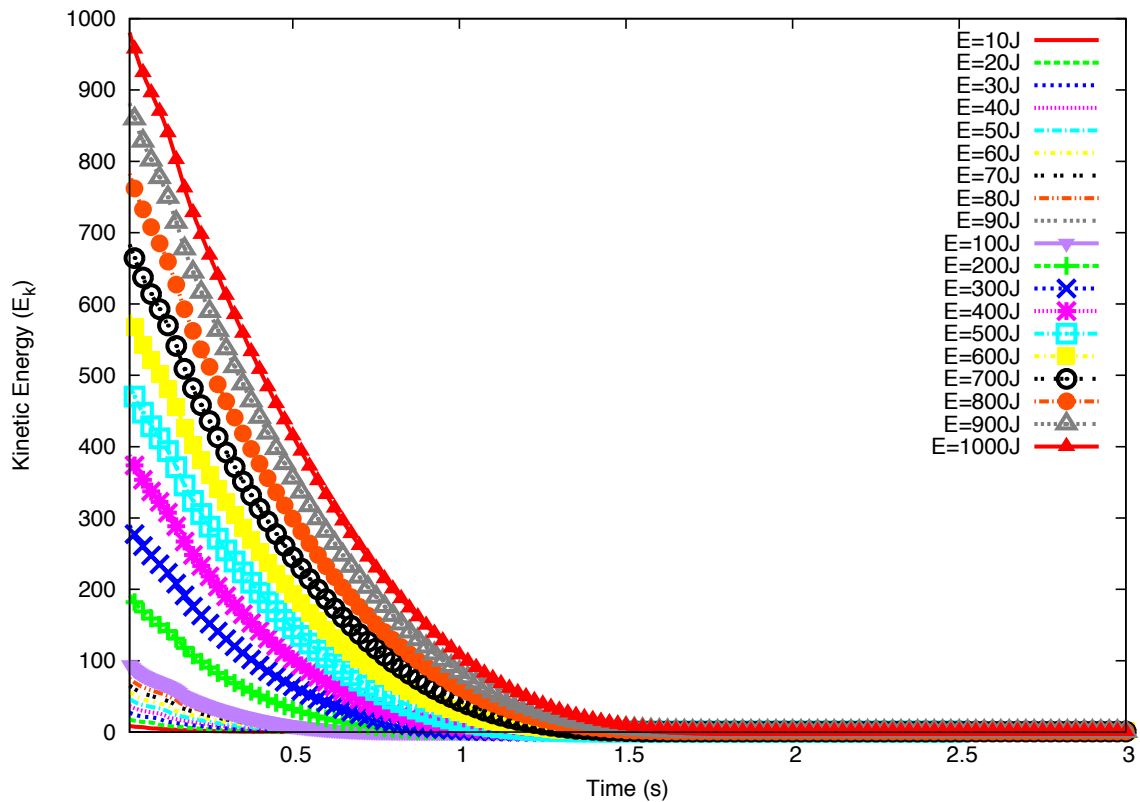
Figure 4.24 Run-out behaviour of a pile subjected to a gradient impact energy

wall and the rolling of the particles down the free surface of the pile and between particles, a fraction of the energy is first transferred to the y component of the velocity field and dissipated during the transient. In this section, we analyse these features in order to arrive in a picture consistent with the evolution of the pile shape.

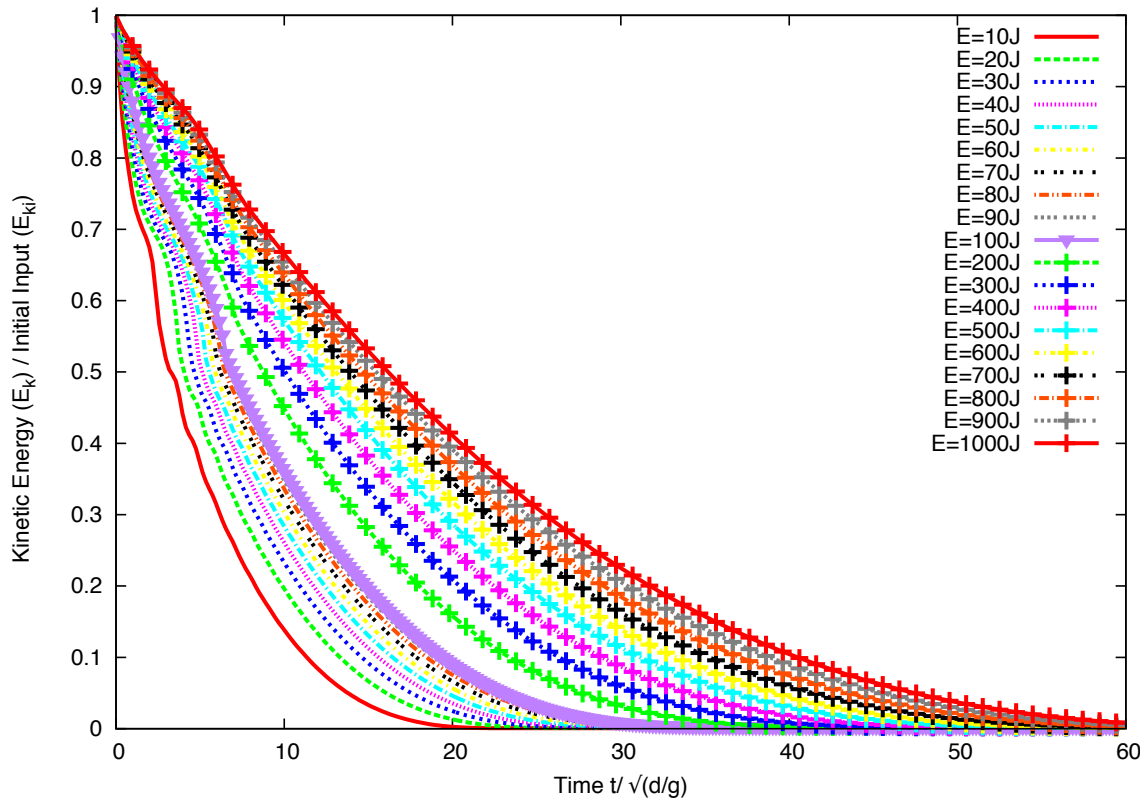
The decay of the total kinetic energy E is displayed in Fig. ??(a) for values of the input energy E_0 . We observe an initial fast drop of E followed by a regular fall-off until the end of the run-out. This regular fall-off occurs clearly with two different functional forms, thus revealing two stages in the evolution of the pile. Fig. ??(b) shows the same plots normalized by E_0 . We see that all plots corresponding to the first regime (low energies) collapse nearly on to a single time evolution. This is consistent with the fact that, as previously shown, in this regime the run-out time t_f is independent of the input energy. In contrast, the plots corresponding to the second regime (high energies) collapse only at the beginning of run-out, i.e. for $t < t_1 \simeq 7.5 (d/g)^{0.5}$.

?? displays the evolution of kinetic energy in the translational (E_x and E_y) and rotational (E_θ) degrees of freedom of the particles. E_x decays as the total energy, but E_y and E_θ increase and pass through a peak before decaying rapidly to a negligibly small level. The transient is best observed for E_y , which has significant values only for $t < t_1$. This energy represents the proportion of kinetic energy transferred to the y component of the velocity field due to the destabilization of the pile and collapse of particles in the cavity behind the pile. We note that the lower E_0 , the higher the peak value of E_y/E_0 . This means that, at low values of the input energy a larger fraction of input energy E_0 is consumed in the destabilization process whereas at a high level of input energy, most of it is dissipated in the spreading phase. For this reason, the total duration t_1 of this destabilization transient is nearly the same in both regimes and its value is controlled by the gravity rather than the input energy. The height of the pile being of the order of 80 d , the total free-fall time for a particle located at this height is $\simeq 12 (d/g)^{0.5}$, which is of the same order as t_1 . As to the rotational energy, its contribution both to the transient stage and spreading appears to be negligible.

To analyze the second phase in the second regime, we now consider only the kinetic energy E'_{x0} available at the end of the transient. This energy is responsible for most of the run-out and hence it is expected to control the run-out distance and time. Fig. ??(a) shows the evolution of E_x normalized by E'_{x0} as a function of time. The plots have seemingly the same aspect but they show different decay times. A decay time τ can be defined as the time required for E_x to decline by a factor 1/2. Fig. ??(b) shows the same data in which the time t' elapsed since t_1 is normalized by τ . Interestingly, now all the data nicely collapse on the same curve. We checked that this curve can not be fitted by simple functional forms such as variants of exponential decay. This means that the spreading of the pile is not a self-similar process in agreement with the fact that the energy fades away in a finite time t'_f .



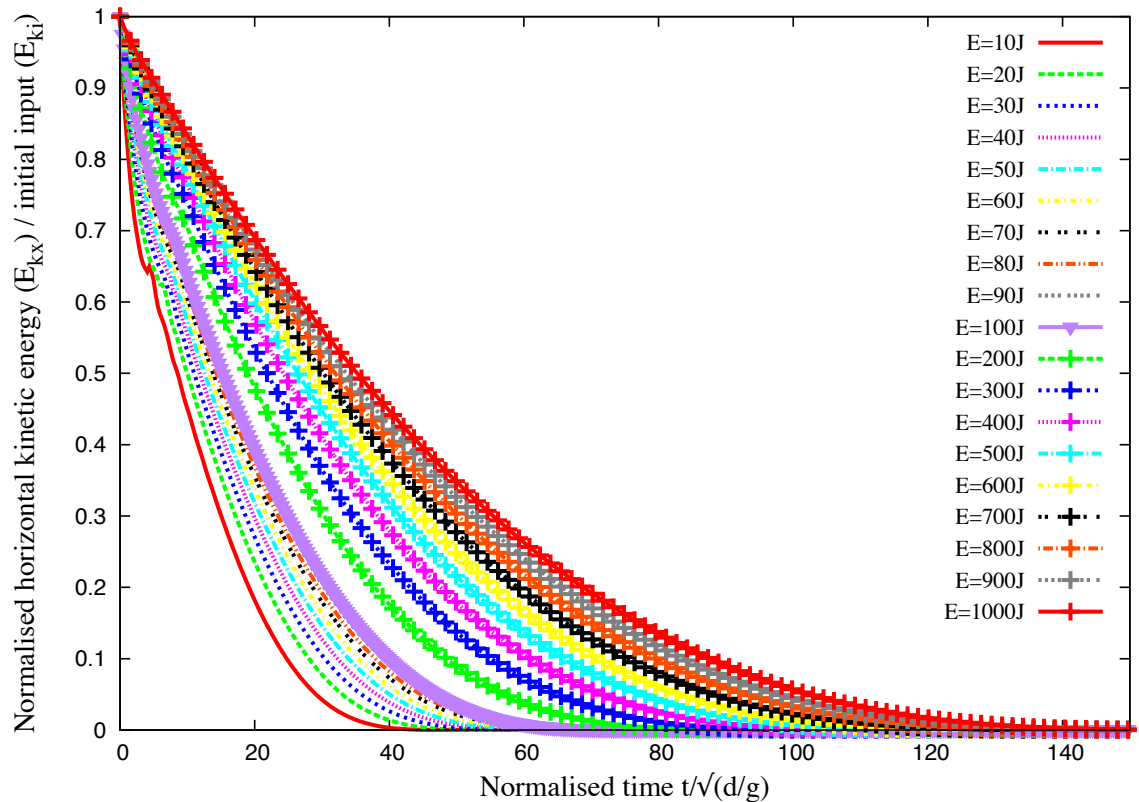
(a) Evolution of total kinetic energy with time



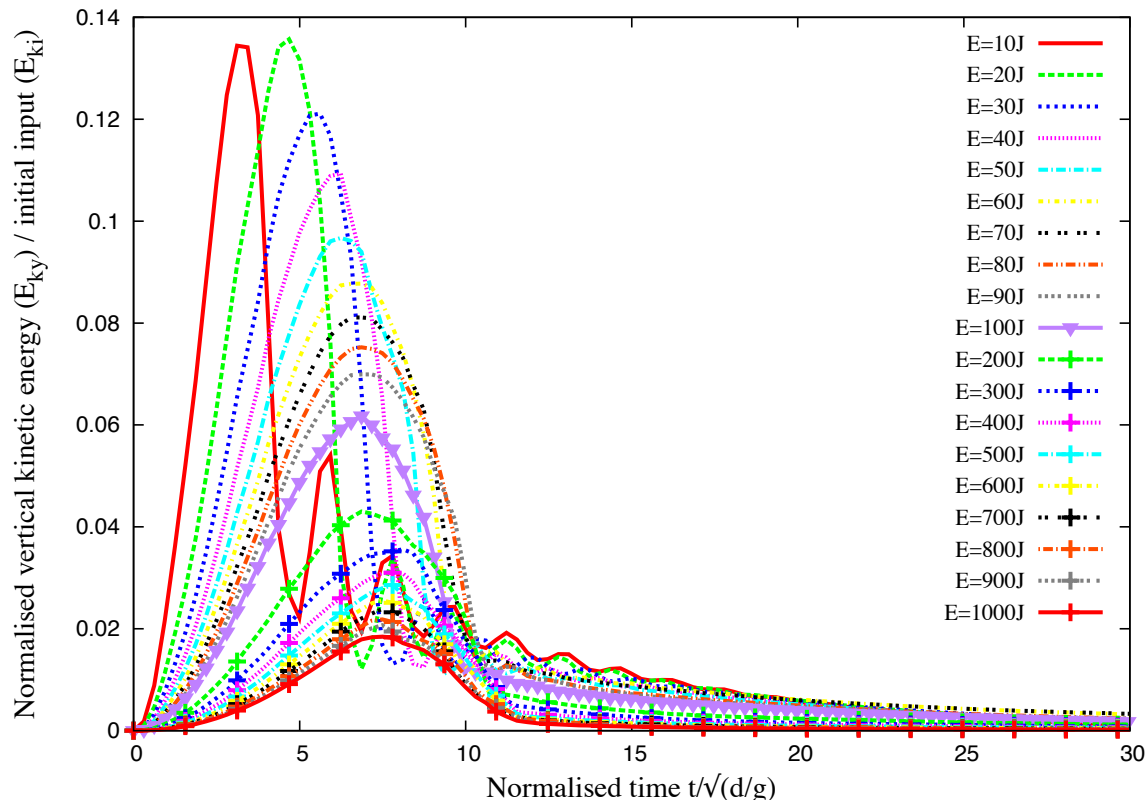
(b) Evolution of normalised kinetic energy with normalised time

Figure 4.25 Evolution of kinetic energy with time

4.3 Slopes subjected to impact loading



(a) Evolution of normalised horizontal kinetic energy with time



(b) Evolution of normalised vertical kinetic energy with time

Figure 4.26 Evolution of vertical and horizontal kinetic energy with time

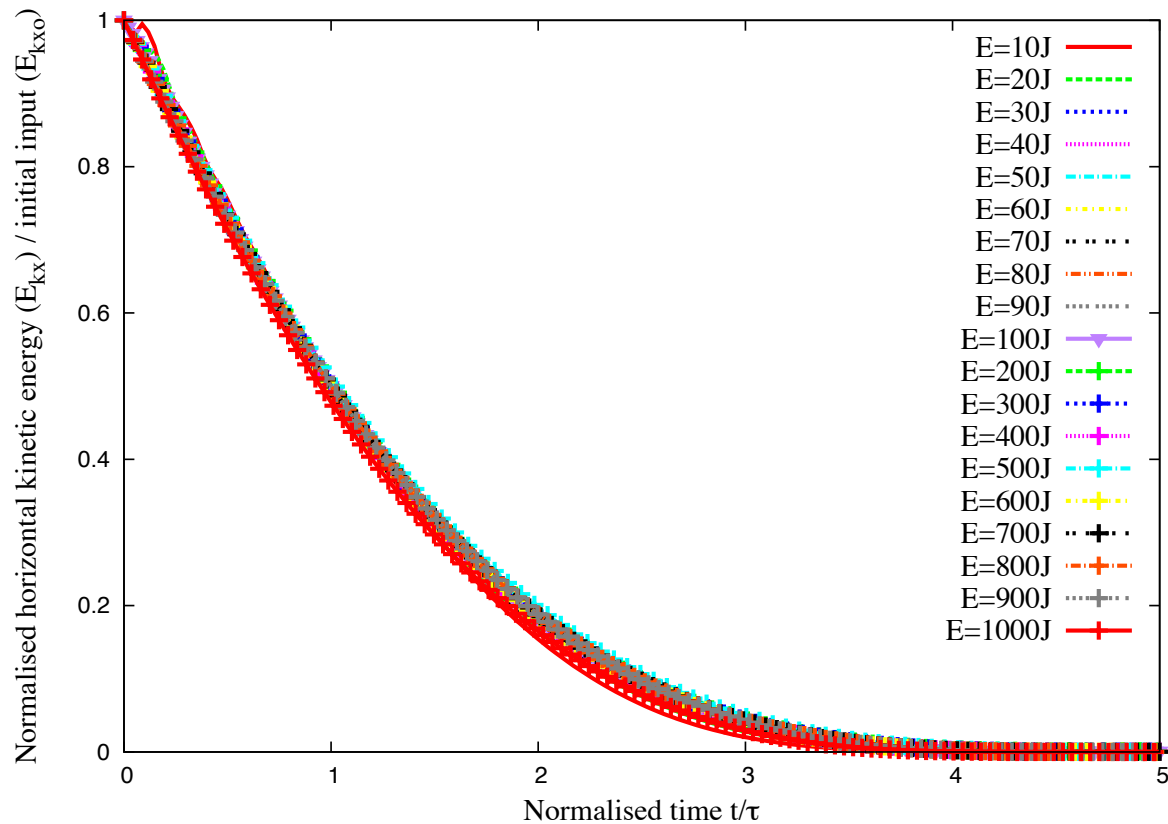


Figure 4.27 Evolution of kinetic energy in the x component of the velocity field normalized by the available kinetic energy at the end of the transient as a function of normalized time.

The scaling of the data with the decay time τ suggests also that the run-out time t'_f since the beginning of the second phase might be a simple function of τ . Figure 4.27 shows both t'_f and τ as a function of E'_{x0} , where we observe a power law for both times over nearly one decade. The run-out time $t'_f \propto (E'_{x0})^{\beta'}$ has the same exponent $\beta' \simeq 0.21 \pm 0.03$ as t_f as a function of E_0 (see Fig. 4.4). For the decay time we have $\tau \propto (E'_{x0})^{\beta''}$ with $\beta'' \simeq 0.28 \pm 0.03$. The relation between the two times can thus be expressed as

$$t'_f = k \tau (E'_{x0})^{\beta'' - \beta'}, \quad (4.11)$$

where $k \simeq 5 \pm 0.4$ and $\beta'' - \beta' \simeq -0.05 \pm 0.06$. This value is small enough to be neglected within the confidence interval of our data. It is therefore plausible to assume that the run-out time is a multiple of the decay time and the spreading process is controlled by a single time. We however note that a weak dependence on the energy E'_{x0} is consistent with the fact that the whole available energy at the beginning of the second phase is not dissipated in the spreading process (calculated from the position of the tip of the pile) since the pile keeps deforming by the movements of the particles at the free surface even when the tip comes to rest. This can explain the small difference between the two exponents as observed here.

4.3.4 Effect of friction

The run-out distance and time and the dissipation of kinetic energy are controlled by the input energy and collective dynamics of the whole pile, as it was analyzed in the previous sections. But they are expected to depend also on the friction. We performed a series of simulations with different values of base friction. The results are shown in Fig. ?? for the profiles of the pile and evolution of the kinetic energy in time. We see no difference in the results for different values of $e_n = e_t$. This is a consequence of the fact that, even at large input energies, the pile remains in a dense state so that multiple collisions inside the pile occur at small time scales compared to the deformation time. When the restitution coefficients are increased, more collisions occur during a longer time interval but the overall energy dissipation rate by collisions remains the same. This effect is a seminal example of collective effects which erase the influence of local parameters at the macroscopic scale. In contrast with the restitution coefficients, however, the effect of the friction coefficient is quite important for the run-out, as observed in Fig. ?? for both the energy decay and geometrical profile of the pile. Both the run-out distance and decay time decrease as the friction coefficient is increased. This effect is much more pronounced at low values of the friction coefficient. The run-out time, for example, is reduced by a factor 4 as μ_s is increased from 0.1 to 0.4 while the run-out times and profiles do not change much for $\mu_s = 0.7$. This “saturation effect” was evidenced in a systematic way in simple shear tests and

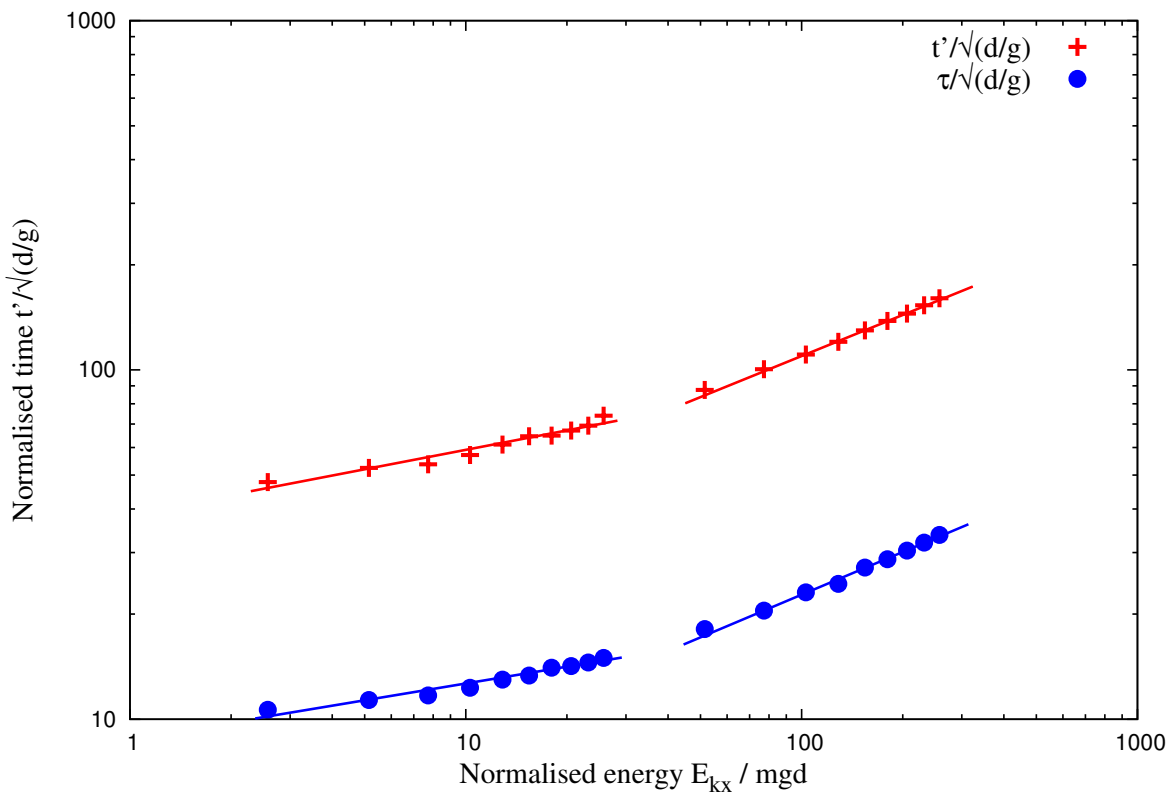
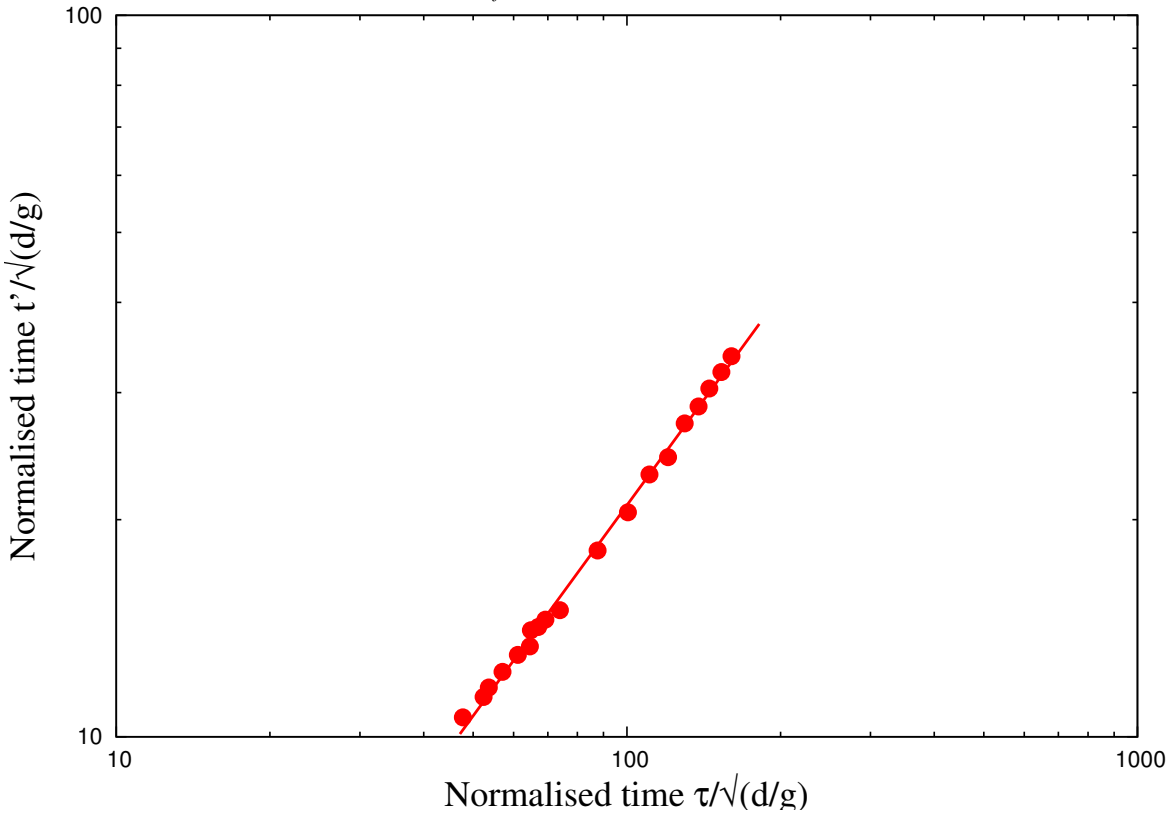
(a) Power law evolution of t'_f and τ as a function of kinetic energy E_{kx0} .(b) Linear relationship between decay time and run-out time after the transient as a function of the normalised kinetic energy E_{kx0} .

Figure 4.28 Decay time and run-out time as a function of the normalised kinetic energy E_{kx0} .

4.4 Summary

45

explained by the observation that the dissipation rate may reach a saturation point where the dilation of the granular material and rolling of the particles change in response to the increase of the friction coefficient [Estrada et al. \(2008\)](#).

Mode of dissipation

The choice of this geometry was motivated by our main goal to focus on the effect of an input energy on the consecutive dynamics of a granular material. For the range of input energies investigated in this pushing test by means of contact dynamics simulations, we observed a power-law dependence of the run-out distance and time with non-trivial exponents. This is a central result of this work as it reveals that the power-law behaviour is a generic feature of granular dynamics. The values of the exponents are not simple functions of the geometry.

We also evidenced two regimes with different values of the exponents: a low-energy regime and a high-energy regime. The first regime reflects mainly the destabilization of the pile by the quake with a run-out time independent of the input energy whereas the second regime is governed by the spreading dynamics induced by the higher value of the input energy. We showed that the evolution of the pile in this high-energy regime can be described by a characteristic decay time and the energy available at the end of the first stage where the pile is destabilized by the quake.

This work may be pursued along two directions: 1) experimental realization of a similar setup with different modes of energy injection and 2) investigating the effect of various particle shapes or the presence of an ambient fluid. Although numerical simulations are generally reliable with realistic results found in the past studies of steady flows, we believe that the transients are more sensitive situations than steady states and the experiments are necessary for checking the validation of the results suggested by the simulations. Provided a convenient method is used for supplying kinetic energy homogeneously into a pile, our configuration is also interesting for the investigation of the behavior of a pile immersed in a viscous fluid.

4.3.5 Effect of material points

27

4.3.6 Comparison with granular column collapse

28

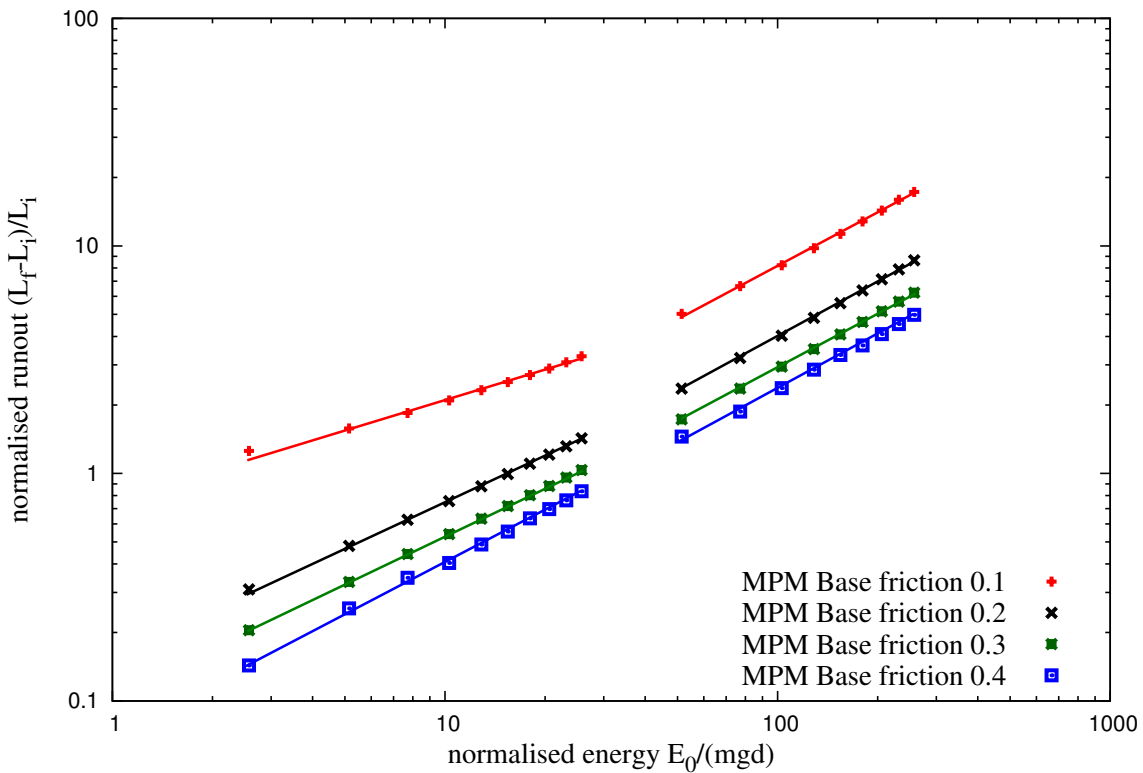
4.4 Summary

29

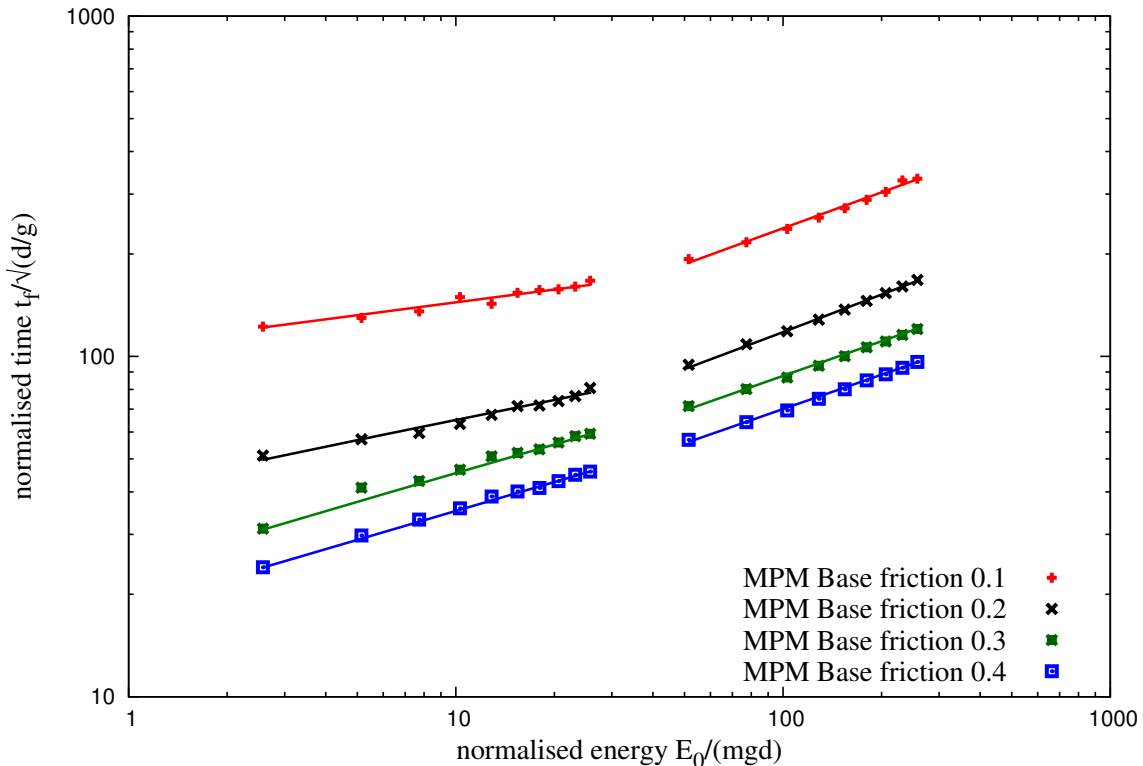
Multi-scale simulation of granular column collapse was performed to understand the ability and limitations of continuum models to capture the micro-mechanics of dense granular flows. The

30

31



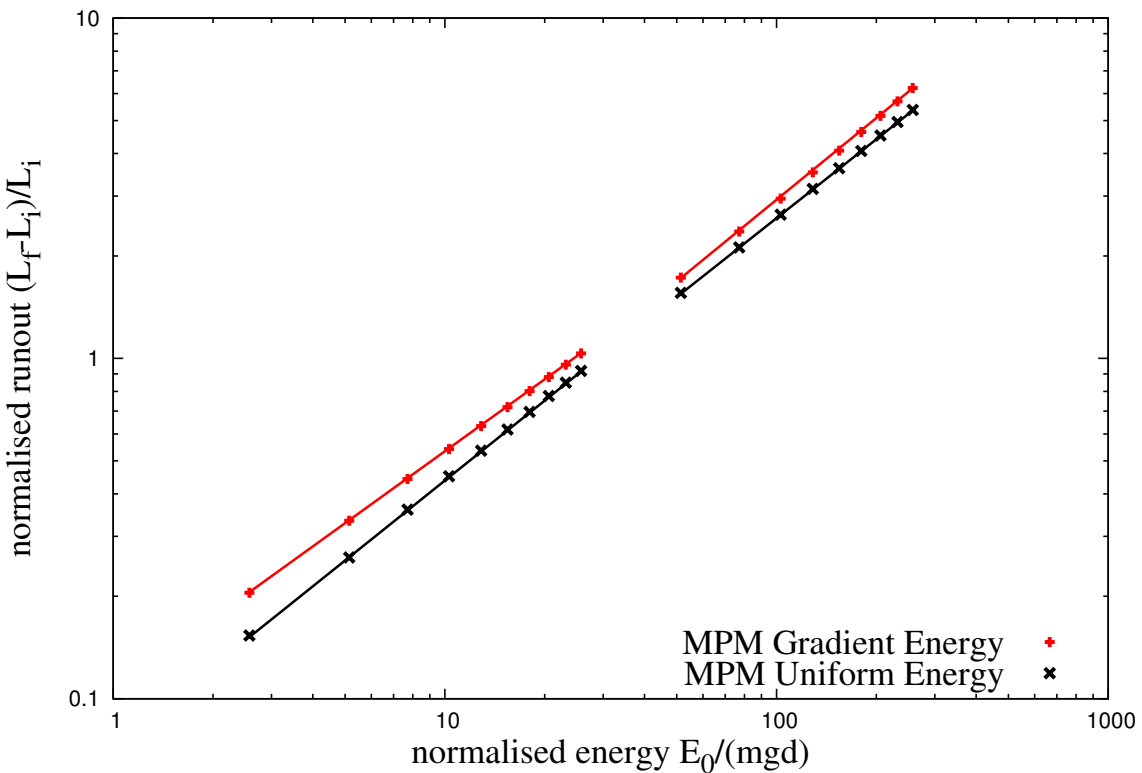
(a) Effect of friction on the run-out distance



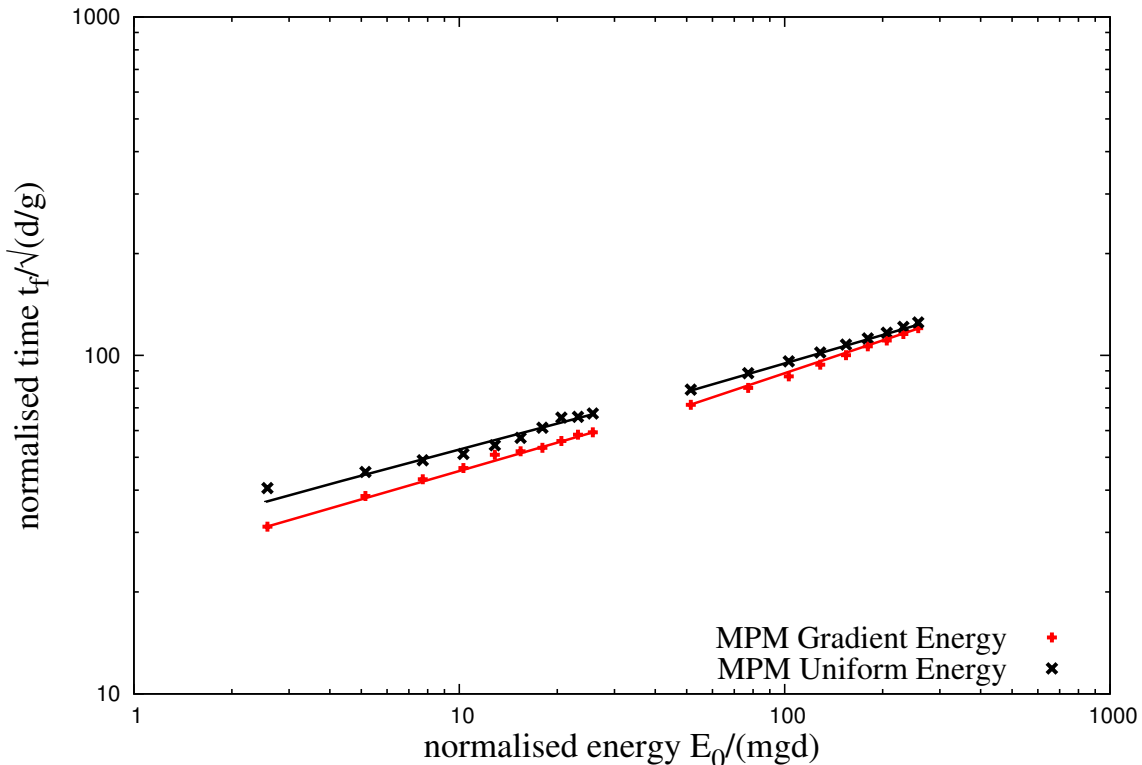
(b) Effect of friction on the duration of run-out.

Figure 4.29 Effect of friction on the run-out behaviour

4.4 Summary



(a) Run-out distance as a function of normalised input kinetic energy



(b) Duration of run-out as a function of normalised input kinetic energy

Figure 4.30 Effect of input velocity distribution on the run-out behaviour

$t = 0 \text{ s}$



$t = 0.03 \text{ s}$



$t = 0.06 \text{ s}$



$t = 0.09 \text{ s}$



Figure 4.31 Snapshots of MPM simulations of the evolution of granular pile subjected to a gradient impact energy $E_0 = 61 \text{ mgd}$.

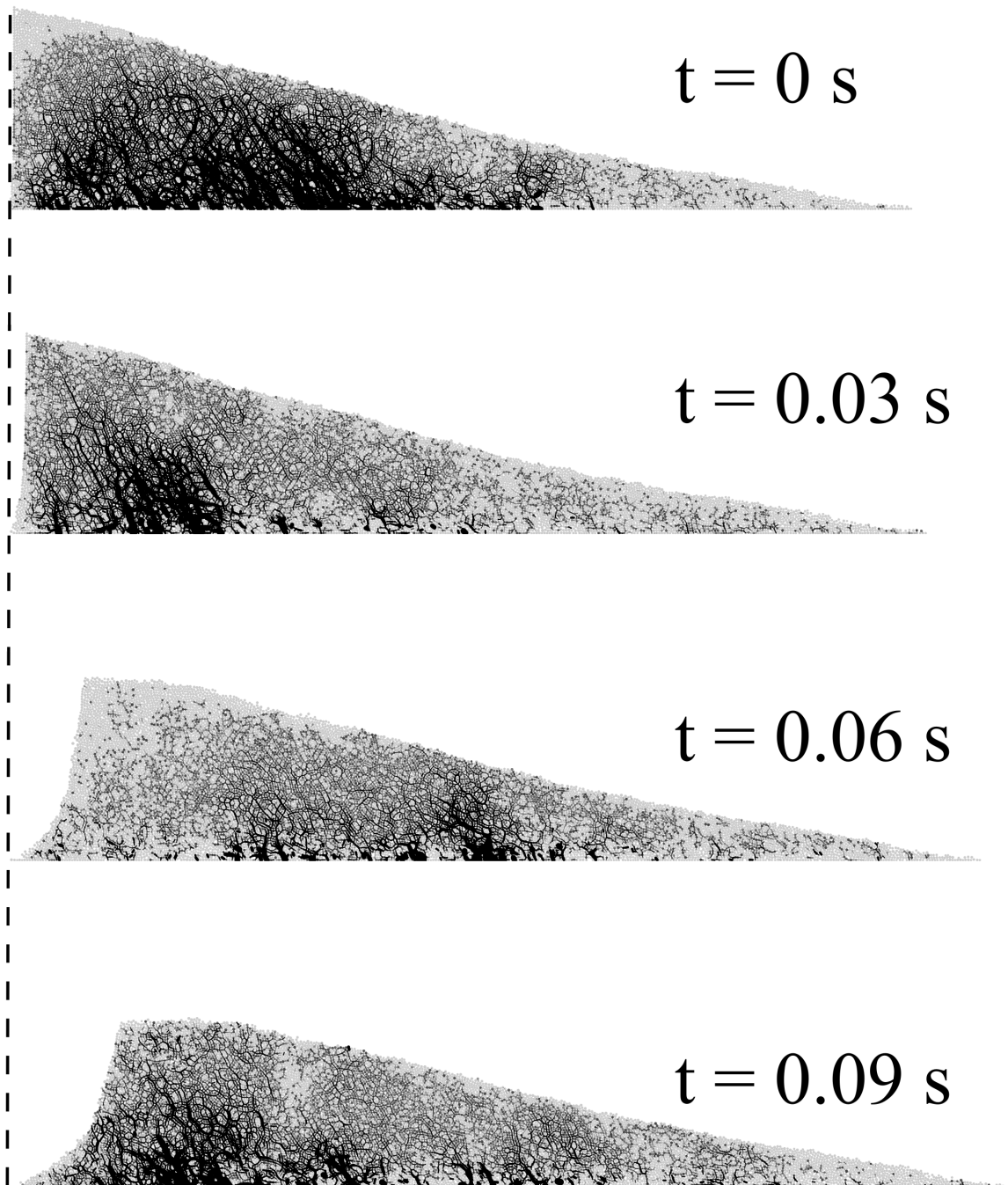


Figure 4.32 Snapshots of DEM simulations of the evolution of granular pile subjected to a gradient impact energy $E_0 = 61 \text{ mgd}$.

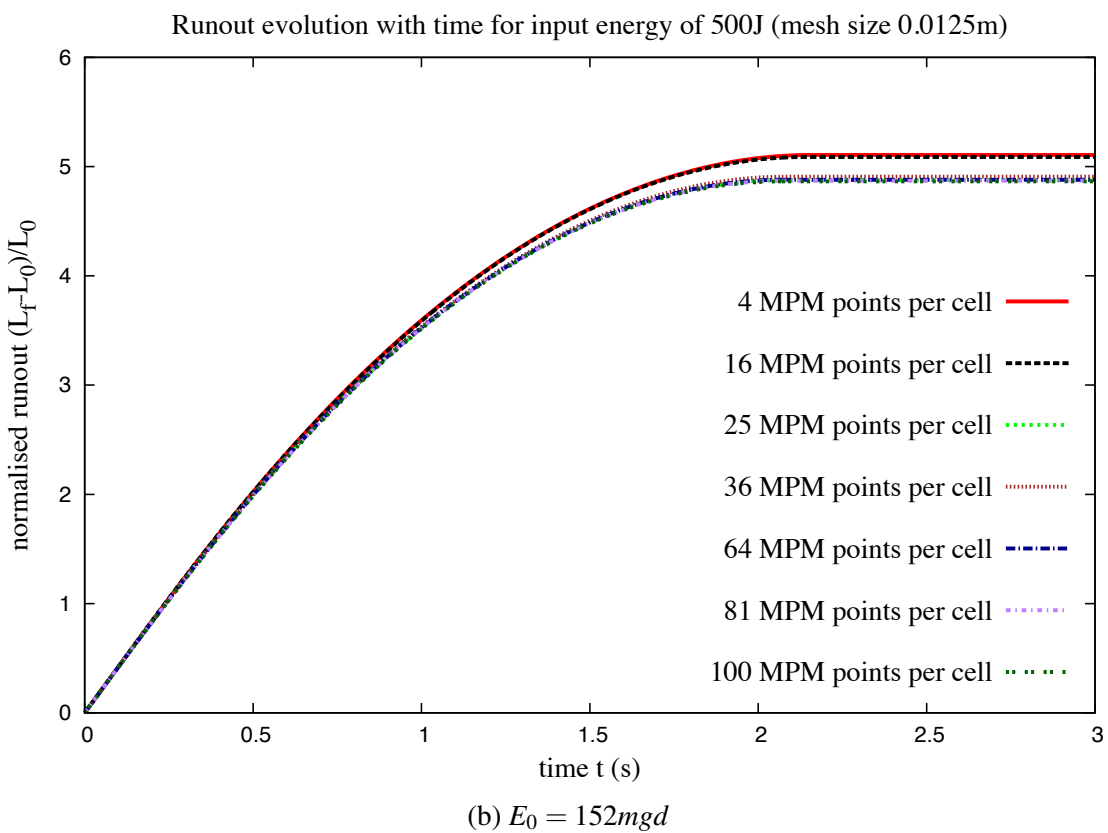
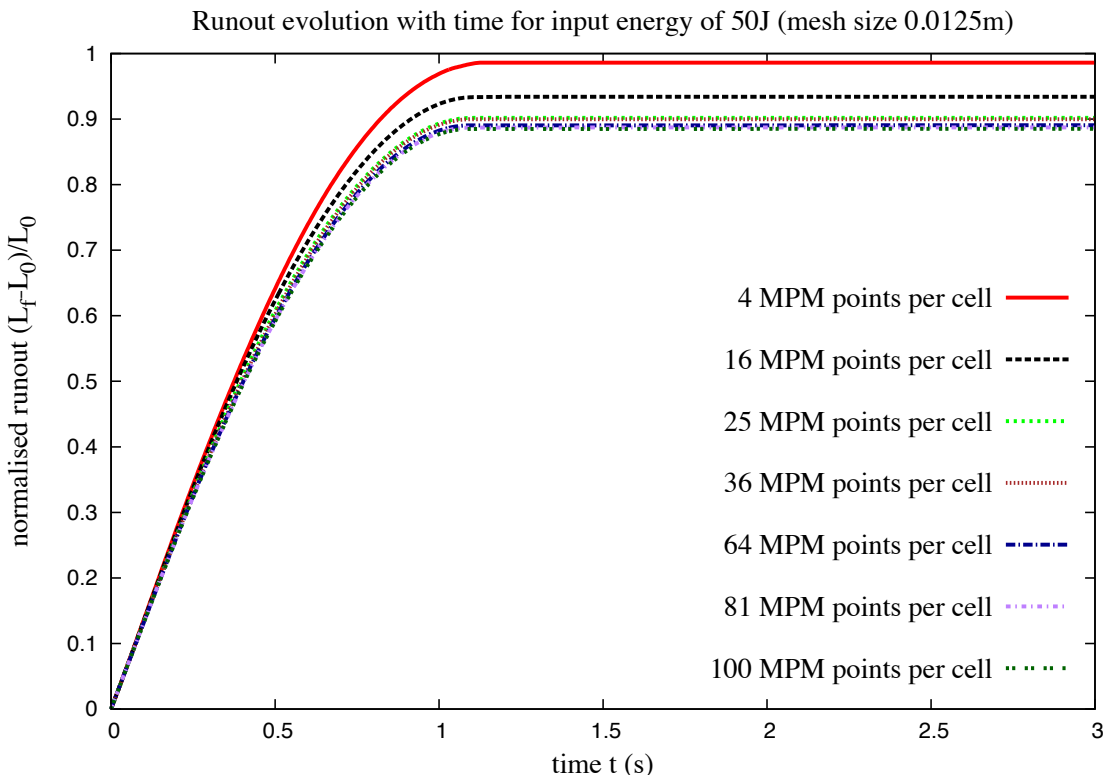


Figure 4.33 Evolution of run-out with time for varying material points per cell.

4.4 Summary

51

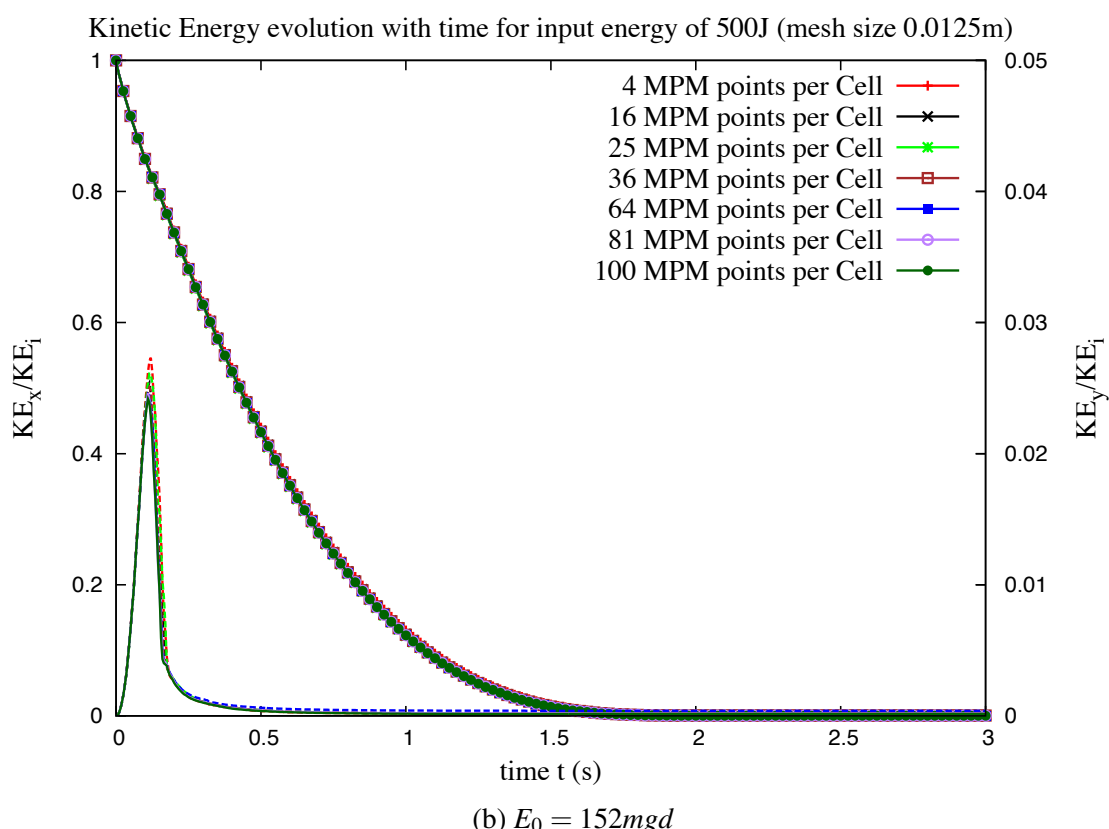
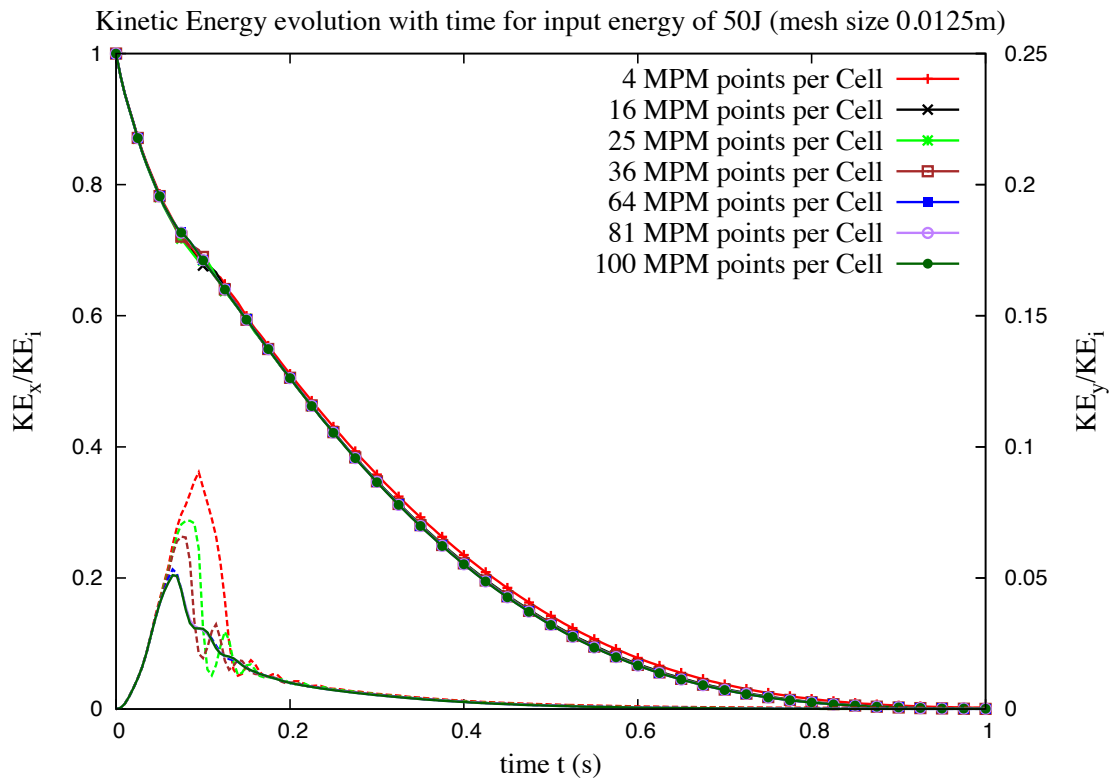


Figure 4.34 Evolution of kinetic with time for varying material points per cell

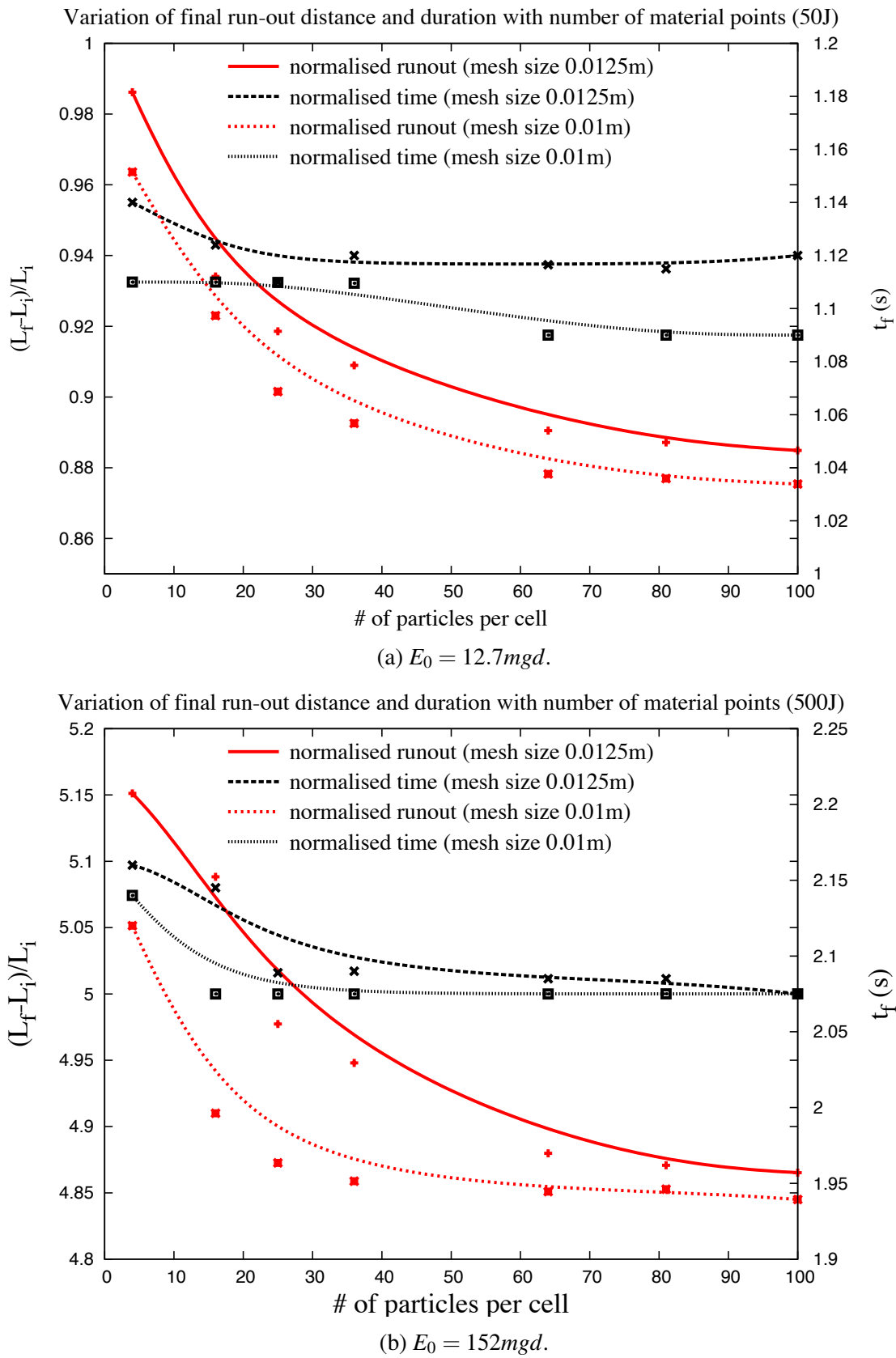


Figure 4.35 Evolution of run-out and duration of flow for varying material points per cell.

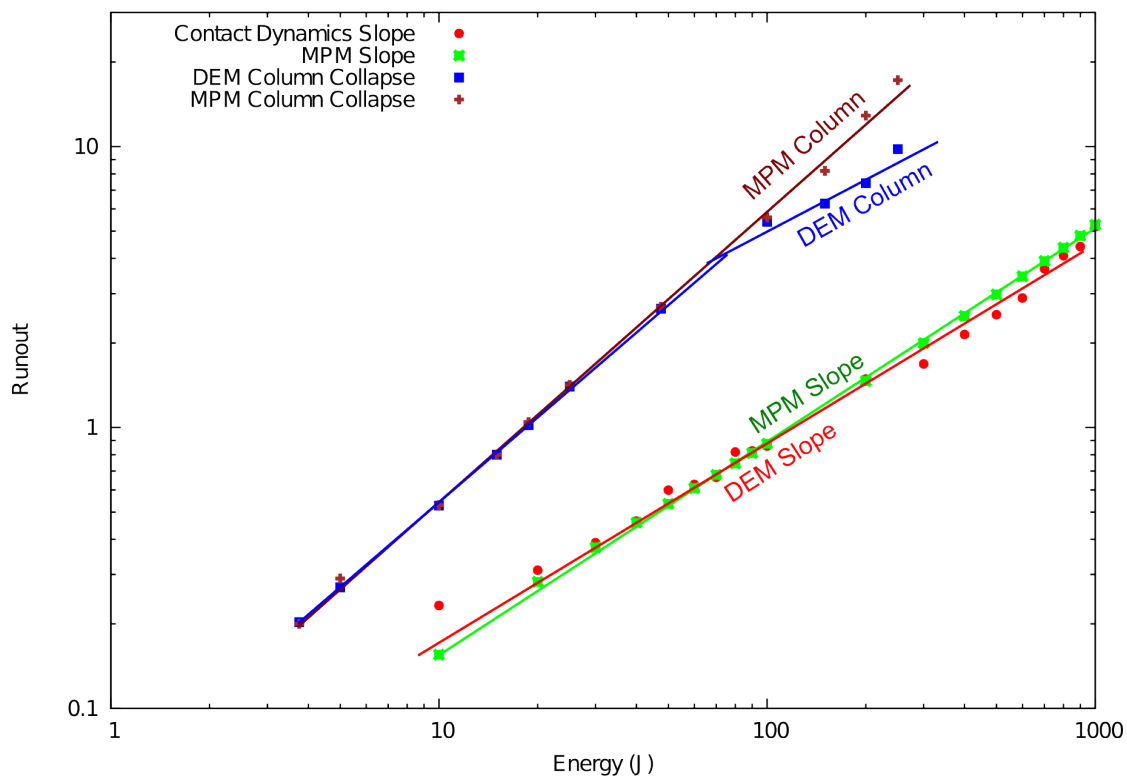


Figure 4.36 Comparison of column collapse with slope subjected to impact loading.

1 run-out behaviour predicted by both continuum and DEM simulations matches for columns
2 with small aspect ratios, where the dissipation is predominantly frictional. However, MPM
3 predicts larger run-out distances for columns with higher aspect ratios. Energy evolution
4 studies using DEM simulations reveal that the run-out behaviour is independent of frictional
5 properties of the granular material and collision predominates the initial free-fall regime. The
6 lack of a collisional energy dissipation mechanism in MPM results in over prediction of run-out
7 distances.

References

- Abe, K., Soga, K., and Bandara, S. (2013). Material Point Method for Coupled Hydromechanical Problems. *Journal of Geotechnical and Geoenvironmental Engineering*, page 04013033. 1
2
3
4
- Balmforth, N. J. and Kerswell, R. R. (2005). Granular collapse in two dimensions. *Journal of Fluid Mechanics*, 538:399–428. 5
6
- Bandara, S. (2013). *Material Point Method to simulate Large Deformation Problems in Fluid-saturated Granular Medium*. PhD thesis, University of Cambridge. 7
8
- Bardenhagen, S. and Kober, E. (2004). The generalized interpolation material point method. *Computer Modeling in Engineering and Sciences*, 5(6):477–496. 9
10
- Cambou, B., Jean, M., and Radjaï, F. (2009). *Micromechanics of granular materials*. Wiley-ISTE. 11
12
- Crosta, G. B., Imposimato, S., and Roddeman, D. (2009). Numerical modeling of 2-D granular step collapse on erodible and nonerodible surface. *J. Geophys. Res.*, 114(F3):F03020. 13
14
- Daerr, A. and Douady, S. (1999). Two types of avalanche behaviour in granular media. *Nature*, 399(6733):241–243. 15
16
- Estrada, N., Taboada, A., and Radjai, F. (2008). Shear strength and force transmission in granular media with rolling resistance. *Physical Review E*, 78(2):021301. 17
18
- Girolami, L., Hergault, V., Vinay, G., and Wachs, A. (2012). A three-dimensional discrete-grain model for the simulation of dam-break rectangular collapses: comparison between numerical results and experiments. *Granular Matter*, pages 1–12. 19
20
21
- Guilkey, J., Harman, T., Xia, A., Kashiwa, B., and McMurtry, P. (2003). An Eulerian-Lagrangian approach for large deformation fluid structure interaction problems, Part 1: algorithm development. *Advances in Fluid Mechanics*, 36:143–156. 22
23
24
- Hogg, A. J. (2007). Two-dimensional granular slumps down slopes. *Physics of Fluids*, 19(9):9. 25
- Iverson, R. M. (1997). The physics of debris flows. *Rev. Geophys.*, 35(3):245–296. 26
- Jean, M. (1999). The non-smooth contact dynamics method. *Computer Methods in Applied Mechanics and Engineering*, 177(3-4):235–257. 27
28
- Kerswell, R. (2005). Dam break with Coulomb friction: A model for granular slumping? *Physics of Fluids*, 17:057101. 29
30

- ¹ Lacaze, L. and Kerswell, R. R. (2009). Axisymmetric Granular Collapse: A Transient 3D Flow
² Test of Viscoplasticity. *Physical Review Letters*, 102(10):108305.
- ³ Lajeunesse, E., Mangeney-Castelnau, A., and Vilotte, J. P. (2004). Spreading of a granular
⁴ mass on a horizontal plane. *Physics of Fluids*, 16(7):2371.
- ⁵ Lajeunesse, E., Monnier, J. B., and Homsy, G. M. (2005). Granular slumping on a horizontal
⁶ surface. *Physics of Fluids*, 17(10).
- ⁷ Larrieu, E., Staron, L., and Hinch, E. J. (2006). Raining into shallow water as a description of
⁸ the collapse of a column of grains. *Journal of Fluid Mechanics*, 554:259–270.
- ⁹ Lo, C. Y., Bolton, M., and Cheng, Y. P. (2009). Discrete element simulation of granular column
¹⁰ collapse. In *AIP Conf. Proc. Powders and Grains 2009*, volume 1145 of *6th International
11 Conference on Micromechanics of Granular Media, Powders and Grains 2009*, pages 627–
¹² 630.
- ¹³ Lube, G., Huppert, H. E., Sparks, R. S. J., and Freundt, A. (2005). Collapses of two-dimensional
¹⁴ granular columns. *Physical Review E - Statistical, Nonlinear, and Soft Matter Physics*,
¹⁵ 72(4):1–10.
- ¹⁶ Mitchell, J. K. and Soga, K. (2005). *Fundamentals of soil behavior*. John Wiley & Sons.
- ¹⁷ Radjai, F. and Dubois, F. (2011). *Discrete-element modeling of granular materials*. ISTE
¹⁸ Wiley, London; Hoboken, N.J.
- ¹⁹ Radjai, F. and Richet, V. (2009). Contact dynamics as a nonsmooth discrete element method.
²⁰ *Mechanics of Materials*, 41(6):715–728.
- ²¹ Rondon, L., Pouliquen, O., and Aussillous, P. (2011). Granular collapse in a fluid: Role of the
²² initial volume fraction. *Physics of Fluids*, 23(7):073301–073301–7.
- ²³ Rycroft, C. H., Orpe, A. V., and Kudrolli, A. (2009). Physical test of a particle simulation
²⁴ model in a sheared granular system. *Physical Review E*, 80(3):031305.
- ²⁵ Schaefer, D. G. (1990). Instability and ill-posedness in the deformation of granular materials.
²⁶ *International Journal for Numerical and Analytical Methods in Geomechanics*, 14(4):253–
²⁷ 278.
- ²⁸ Staron, L. and Hinch, E. J. (2006). The spreading of a granular mass: role of grain properties
²⁹ and initial conditions. *Granular Matter*, 9(3-4):205–217.
- ³⁰ Staron, L. and Hinch, E. J. (2007). The spreading of a granular mass: Role of grain properties
³¹ and initial conditions. *Granular Matter*, 9(3-4):205–217.
- ³² Staron, L. and Lajeunesse, E. (2009). Understanding how volume affects the mobility of dry
³³ debris flows. *Geophys. Res. Lett.*, 36(12):L12402.
- ³⁴ Staron, L., Radjai, F., and Vilotte, J. P. (2005). Multi-scale analysis of the stress state in
³⁵ a granular slope in transition to failure. *The European physical journal. E, Soft matter*,
³⁶ 18(3):311–20.

- Topin, V., Monerie, Y., Perales, F., and Radjaï, F. (2012). Collapse Dynamics and Runout of Dense Granular Materials in a Fluid. *Physical Review Letters*, 109(18):188001. 1
2
- Utili, S., Zhao, T., and Houlsby, G. (2014). 3D DEM investigation of granular column collapse: 3
Evaluation of debris motion and its destructive power. *Engineering Geology*. 4
- Warnett, J. M., Denissenko, P., Thomas, P. J., Kiraci, E., and Williams, M. A. (2013). Scalings 5
of axisymmetric granular column collapse. *Granular Matter*, 16(1):115–124. 6
- Zenit, R. (2005). Computer simulations of the collapse of a granular column. *Physics of Fluids*, 7
17(Compendex):031703–1–031703–4. 8